Composites Part B 302 (2025) 112472



Contents lists available at ScienceDirect

Composites Part B

journal homepage: www.elsevier.com/locate/composites





Experimental characterization of mechanical and tribological properties of composite materials for friction-based force-limiting structural components

Kaixin Chen [a,*], Georgios Tsampras [a], Shivaglal Cheruvalath [b], Mary Thundathil [c]

[a] Department of Structural Engineering, University of California San Diego, 9500 Gilman Drive, La Jolla, 92093, CA, USA
[b] SLC Friction Materials & Plastic Laminates LLC, Menomonee Falls, WI, USA
[c] Scan-Pac Mfg., Inc., N84 W13480 Leon Road, Menomonee Falls, 53051, WI, USA

ARTICLE INFO

Keywords:
Composite materials
Experimental testing
Tribology
Friction-based structural components
Earthquake structural engineering

ABSTRACT

This paper presents an experimental study to characterize the mechanical properties of composite materials and the tribological properties of composite to low-carbon structural steel friction interfaces for friction-based structural components in earthquake structural engineering applications. A systematic experimental testing program was developed, including the coupon tensile test, the plate bearing test, the bolt relaxation test, and the friction test. The friction test considered the normal load level, loading frequencies, sliding velocities, velocity profiles, and sliding histories as the testing parameters. Six types of phenolic-resin-based fiber-reinforced composite materials were tested. The results revealed the influence of the manufacturing process and the constituents of the composite materials on their mechanical and tribological properties. The flash compression molding process in manufacturing could produce composite materials having a lower concentration of phenolic resin than designed, and these materials exhibited exacerbated through-thickness creep behavior. Friction tests with different sliding velocities showed a general trend where an increase in the sliding velocity overall reduced the coefficient of friction, while lower sliding velocities overall increased the coefficient of friction. The velocity-dependent frictional behavior was found to depend on the material constituents of the composite materials. Among the friction interfaces tested, the friction interface with the composite friction material Gatke 398 (containing glass reinforcing fibers and graphite, Teflon and molybdenum disulfide MoS_2 lubricants) in contact with low-carbon structural steel appeared to exhibit the most stable frictional behavior under various sliding velocities and was considered suitable for use in friction-based structural components for earthquake structural engineering applications.

1. Introduction

1.1. Friction-based structural components and friction interfaces

Over the past five decades, friction-based structural components have been extensively developed by structural engineers and have been used in various structural applications for seismic response modification purposes. The use of friction-based structural components in structural applications is commonly considered to be of two types: (1) between the superstructure and the foundation, friction pendulums have been used as base isolators, and (2) for superstructures, friction-based structural components have been designed as primary structural connections, for example, force-limiting connections between floors and walls [1], or as supplemental energy dissipation devices [2]. Chen et al. [3] summarized the use of friction-based structural components in superstructures, categorized by applications in different types of structural systems. Jaisee et al. [4] summarized the use of these components as dampers, categorized by damper configurations. The mechanics of friction-based structural components always involves the relative movement between two surfaces that are in contact due to an applied normal pressure. The contact interface between these two surfaces is known as the friction interface. The response of a friction-based structural component depends on the friction force generated at the friction interface. Hence, the characterization and selection of materials that form the friction interface are important to ensure a desired response of the friction-based structural component. For friction pendulums, the source of the normal load acting on the friction interface comes from the self-weight of the superstructure. Therefore, a desired response of friction pendulums can be achieved by using material pairs with low coefficients of friction, for example, Teflon in contact with polished

* Corresponding author.
E-mail addresses: kac011@ucsd.edu (K. Chen), gtsampras@ucsd.edu (G. Tsampras).
URL: https://tsampras.ucsd.edu/about-us (G. Tsampras).

https://doi.org/10.1016/j.compositesb.2025.112472
Received 11 February 2025; Received in revised form 29 March 2025; Accepted 30 March 2025
Available online 11 April 2025
1359-8368/© 2025 The Authors. Published by Elsevier Ltd. This is an open access article under the CC BY-NC-ND license (http://creativecommons.org/licenses/by-nc-nd/4.0/).

stainless steel [5], which provides a coefficient of friction of less than 0.2. For friction-based structural components in superstructures, the source of the normal load acting on the friction interface usually comes from prestressed components such as pretensioned structural bolts. The efficient design of friction-based structural components for superstructure applications requires material pairs that result in sliding interfaces with higher coefficients of friction. Otherwise, the number of prestressed components required to provide the normal load could be excessive and impractical to design. This paper focuses on material characterization for friction-based structural components for superstructure applications. The discussion related to friction pendulums is beyond the scope of this paper.

1.1.1. Bimetallic friction interfaces

Research has been conducted to characterize material pairs for friction interfaces of friction-based structural components for earthquake structural engineering applications. Bimetallic friction interfaces have been widely studied. FitzGerald et al. [6] applied steel-steel faying surfaces in slotted-bolted connections for concentrically braced frames. Tremblay [7] tested faying surfaces of five types of materials and their combinations, including four types of steel-based alloys and one type of cobalt-based alloys. Grigorian et al. [8] tested low-carbon structural steel to low-carbon structural steel and low-carbon structural steel to brass friction interfaces. The experimental results [8] showed that low-carbon structural steel to brass friction interfaces generated relatively constant friction forces and thus were considered more suitable for earthquake structural engineering applications. Low-carbon structural steel to brass friction interfaces were also tested in [1,9–13] for various earthquake structural engineering applications. Although in [8] it was shown that low-carbon structural steel to low-carbon structural steel friction interfaces generated friction forces having fairly large variations, solutions have been proposed, including treating the low-carbon structural steel plate surface with thermally sprayed aluminum [12] or using hardened abrasion-resistant steel such as Bisalloy [11,14], to improve the response of steel-steel friction interfaces. Other bimetallic friction interfaces that have been characterized for earthquake structural engineering applications include: low-carbon steel to titanium [10]; low-carbon steel to brown copper [15]; stainless steel and alloy cast steel to leaded bronze [16]; and low-carbon steel to aluminum [11,13].

The main challenge of using bimetallic friction interfaces is galvanic corrosion induced at the friction interface from the contact between dissimilar metals. For bimetallic friction interfaces, galvanic corrosion generates rust in long-term operation and alters the properties of the friction interface. Chan and Tang's experiment [17] showed that compared with a rust-free polished condition, the coefficient of friction of a bimetallic friction interface with rust can be reduced by 50%. Another challenge associated with bimetallic friction interfaces, as discussed in ASCE/SEI 7-22 Commentary C18.2.4.1 [18], is that the coefficient of friction may increase substantially over time due to cold welding at the friction interface. Because of galvanic corrosion and cold welding at the friction interface, ASCE/SEI 7-22 Commentary C18.2.4.1 made the following statement: "*all bimetallic interfaces result in significant changes in friction force over time that are not possible to predict, and therefore, these types of interfaces should not be used.*". Hence, if bi-metallic friction interfaces are used, their long-term performance should be further evaluated.

1.1.2. Composite-metallic friction interfaces

Composite-metallic friction interfaces are considered alternatives to bimetallic friction interfaces because they are less vulnerable to galvanic corrosion problems. The characterization of composite-metallic friction interfaces has been conducted for various earthquake structural engineering applications. Lie [19] used composite-metallic friction interfaces in earthquake energy absorbers. Three types of composites (Ferrobestos: DM1, DM6, and AS10) were tested, and the metallic surface was made of stainless steel. Testing parameters in this study included the normal load level, loading frequencies, and the working temperature of the energy absorber (room temperature vs. freezing temperature). Lie [19] reported that the composite-metallic friction interfaces had satisfactory and consistent responses within the range of normal load levels and loading frequencies that were tested, at both room and freezing temperatures.

Tyler [20] tested a friction damper with the composite to bright-drawn mild steel friction interface and the composite material was a type of brake lining. Testing parameters in this study included the normal load level, sliding velocities, and number of loading cycles. Tyler [20] concluded that the composite-metallic friction interface tested in this study had a fairly large difference between the static and dynamic coefficients of friction, and hence it required further investigation. In addition, a loss of friction force of 20% was observed after 20 cycles of loading, and the loss was attributed to the wear of the brake lining material.

Chi and Uang [10] tested the composite (AFT200) to low-carbon structural steel friction interface for a slotted-bolted connection. Eight test runs were completed. Chi and Uang [10] concluded that the composite-metallic friction interface tested in this study exhibited satisfactory and repeatable performance and outperformed other bimetallic friction interfaces tested in the same study.

Kim and Christopoulos [21,22] tested six composite-metallic friction interfaces for use in friction damped posttensioned self-centering steel moment-resisting frames. The combinations of three types of composites (NF-916, NF-780, and NF-336) and two types of metallic materials (mild steel and stainless steel) were considered. Testing parameters in this study included the normal load level, loading frequencies, sliding histories, and the configuration of the tested connection (one bolt vs. two bolts). The experimental testing results showed that the friction interfaces with the composite material NF-916 exhibited a stable and repeatable frictional behavior, and therefore Kim and Christopoulos [21,22] suggested using the NF-916 to stainless steel friction interface for the beam–column connection proposed in their study.

Golondrino et al. [23] tested the composite (D3923) to low-carbon structural steel friction interface for asymmetrical friction connections. Testing parameters were loading frequencies, and moreover, three configurations of the composite material pad were considered. Experimental results showed that the friction interface between the composite (D3923) and the low carbon structural steel led to effectively constant friction force during sliding. The connection tested exhibited degradations in the sliding friction force of more than 5% and the degradation was attributed to loss of bolt tension due to wear of the composite material (D3923).

Latour et al. [12] tested three composite-metallic friction interfaces for supplemental damping devices. The composite materials were three types of rubber materials (named M0, M1, and M2 in the study) and the metallic surface was made of low-carbon structural steel. Testing parameters in this study included the normal load level and the number of loading cycles. In addition, this study tested two types of bolt washers, i.e., circular flat steel washers and packets of steel disc springs. Out of the three composite materials tested, Latour et al. [12] concluded that Material M0 exhibited a very stable behavior even under a high level of normal load; Material M1 exhibited pinching behavior, a low friction coefficient and rapid degradations; and Material M2 exhibited a very stable behavior but the coefficient of friction was quite low. Latour et al. [12] considered Material M0 suitable for their applications.

Tsampras et al. [1,24] characterized three composite-metallic friction interfaces for use in force-limiting connections between floors and seismic force resisting building systems. The composite materials tested were AFT200, RF42, and Gatke 398, and the metallic surface was made of low-carbon structural steel. Testing parameters in this study included the normal load level, loading frequencies, sliding velocities, velocity profiles (earthquake vs. sinusoidal), and sliding histories. The

responses of friction devices manufactured with different machining tolerances were also compared. Tsampras et al. [1] observed that due to the break-in effect, the coefficient of friction of the composite-metallic friction interface at the beginning of sliding increased when the cumulative displacement increased. In the test of the composite (Gatke 398) to low-carbon structural steel friction interface, the sliding force exhibited an increase in tests with fairly low sliding velocities and a decrease in dynamic tests. Tsampras et al. [1] used Bowden and Tabor's adhesive friction theory [25] to explain the observed velocity-dependent sliding force variation. Although dwell time was not listed as a testing parameter, Tsampras et al. [1] observed that dwell time between tests permitted rejuvenation of the friction interface, characterized by an increase in the sliding force. Tsampras et al. [1,24] also reported that there was no correlation between the temperature variation and the sliding force variation. The tested composite (Gatke 398) to low-carbon structural steel friction interface was considered suitable for applications in floor-to-wall force-limiting connections [1].

Li et al. [26] tested four composite-metallic friction interfaces. The combinations of two types of composites (non-asbestos organic (NAO) NAO780, and Polytetrafluoroethylene (PTFE)) and two types of metallic materials (mill steel and stainless steel) were considered. Testing parameters in this study included the normal load level, loading frequencies, and sliding velocities. Experimental results showed that NAO-steel friction interfaces exhibited higher coefficients of friction, while PTFE-steel friction interfaces exhibited more stable frictional behavior.

Paronesso and Lignos [27] characterized five composite-metallic friction interfaces for sliding friction dampers using the design of the friction-based force-limiting connections proposed by Tsampras et al. [1]. The composite materials were named M1, M2, M3, M4, and M5 in the study and the metallic surface was made of low-carbon structural steel. Testing parameters in this study included the normal load level, loading frequencies, sliding velocities, velocity profiles, and sliding histories. Paronesso and Lignos [27] suggested that materials M1 and M4 were more suitable for use in friction dampers because they exhibited fairly invariant coefficients of friction under different levels of normal pressure and at different sliding velocities. Materials M2 and M3 induced a significant loss of bolt pretension, and the loss was attributed to the processing of these two materials. The material M3 also exhibited a normal pressure-dependent coefficient of friction. The material M5 was not recommended due to its high wear rate and the observed failure of the friction shim during the test. Paronesso and Lignos [27] also reported that for earthquake structural engineering applications, the coefficients of friction of materials M1 and M4 can be practically assumed to be temperature independent.

Similar to Li et al. [26], Gao et al. [28] tested two composite-metallic friction interfaces, considering two types of composite materials, NAO and PTFE, and the metallic surface was made of low-carbon structural steel. Testing parameters in this study included the normal load level, loading frequencies, sliding velocities, and sliding histories. Gao et al. [28] considered four configurations of the test setup for improved connection performance. Gao et al. [28] observed that both NAO-steel and PTFE-steel friction interfaces exhibited velocity-dependent frictional behavior and that the coefficients of friction for both friction interfaces under high-speed loading were reported to be "significantly greater" than those under low-speed loading. Similar to Tyler [20] a difference between static and dynamic coefficients of friction was observed in this study [28] and the difference was reported to be less than 10% with the increase of loading frequencies. The reusability of the friction interfaces was also assessed in this study.

In summary, the following parameters are typically considered in characterizing the response of composite-metallic friction interfaces for earthquake structural engineering applications: the normal load level, loading frequencies, sliding velocities, sliding histories, velocity profiles, and parameters related to the friction-based component itself, including configurations and machining parameters. Although temperature has been considered an important parameter for other tribological applications such as automotive applications [29], it is not considered as important for composite to low-carbon structural steel friction interfaces used in friction-based structural components for earthquake structural engineering applications [1,27].

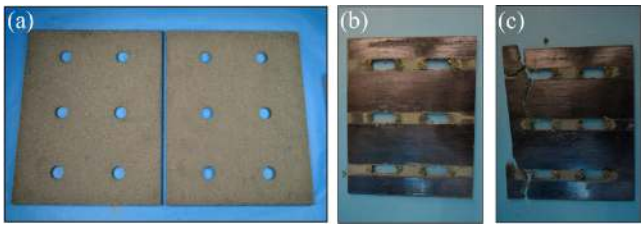


Fig. 1. Photos of RF42 friction shims from [24] (a) Friction shims before the test (b) Damaged friction shim with elongated bolt holes (c) Damaged friction shim with elongated bolt holes associated with net section tensile failure.

1.2. Additional considerations related to composite-metallic friction interfaces

1.2.1. Mechanical strengths of composite materials

Past studies listed in Section 1.1.2 focused primarily on the tribological properties of the composite-metallic friction interface. Although discussions about the mechanical properties of composite materials were limited in those studies, damages of composite material friction shims were observed in previous experimental tests of friction-based structural components with composite-metallic friction interfaces [1,24,27,30]. Fig. 1 shows photos of example damaged friction shims made of the composite material RF42 from previous experimental tests [24].

In [1,24,27,30], damages of composite material friction shims were due to the bearing action between friction shims and pretensioned structural bolts. Figs. 2 and 3 explain the mechanics of this bearing action. Fig. 2 presents an example friction-based structural component that has a slotted-bolted configuration, which is one of the most commonly studied configurations of friction-based structural components. The example slotted-bolted friction-based structural component consists of two clamping plates, two friction shims, one sliding plate, and six structural bolts and bolt assemblies (nuts and washers). Structural bolts and bolt assemblies clamp the clamping plates, friction shims, and the sliding plate together and provide the normal load acting on the friction interface between friction shims and the sliding plate. In a seismic event, the friction shims are expected to slide against the sliding plate and remain relatively static to the clamping plates.

Fig. 3(a) shows the ideal load path of the example slotted-bolted friction-based structural component in Fig. 2. For this component, the total normal load provided by six structural bolts and bolt assemblies is termed N. The coefficient of friction between the friction shims and the clamping plates is termed μ_1. The coefficient of friction between the friction shims and the sliding plate is termed μ_2. According to the Coulomb's friction equation [31], a friction force $f = 2\mu_2 N$ is generated by this component. In an ideal situation, assuming that the clamping plates and the sliding plate are made of the same material, and without considering the break-in effect, μ_1 is equal to μ_2. For the friction shim, the friction force generated between the surface in contact with the clamping plate is equal to the friction force generated between the surface in contact with the sliding plate. The friction shim is thus under pure in-plane shear in the direction of sliding.

In practice, the break-in effect of the friction interface will affect the load path of the slotted-bolted friction-based structural component. Fig. 3(b) shows a schematic pattern of the break-in effect that has been observed in past experimental tests [1], represented by an increase in the coefficient of friction from μ_1 to μ_2 given an increase in the

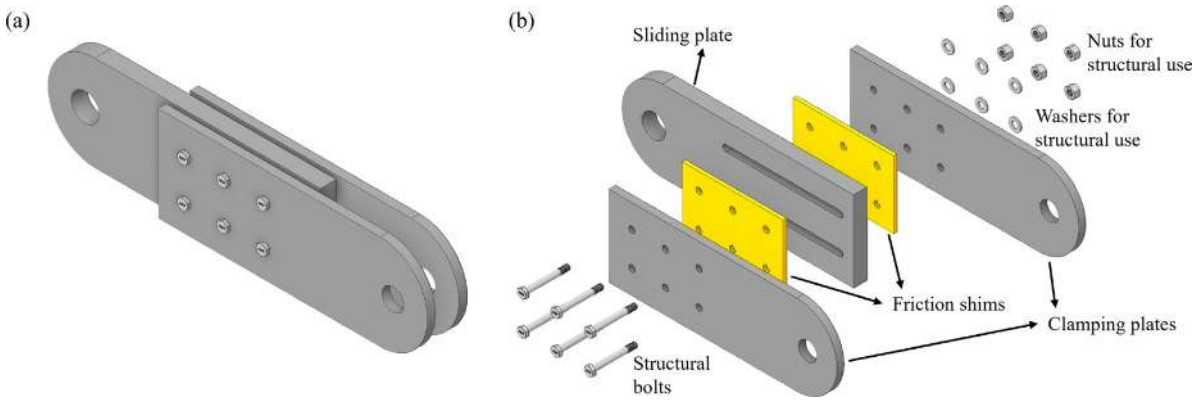


Fig. 2. (a) A schematic representation of an example slotted-bolted friction-based structural component; prototype adopted from [1] (b) Exploded view of the example slotted-bolted friction-based structural component.

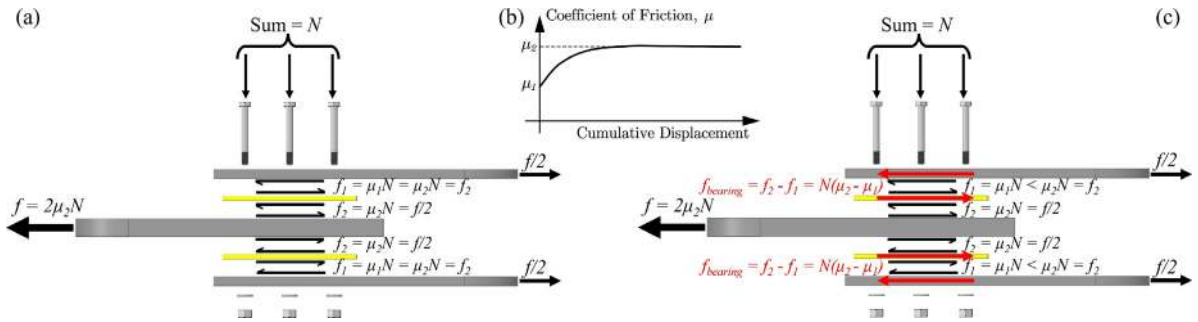


Fig. 3. (a) Ideal load path of the example slotted-bolted friction-based structural component in Fig. 2 (b) A schematic representation of the break-in effect reported in [1] (c) Load path of the example slotted-bolted friction-based structural component considering the break-in effect of the friction interface.

cumulative displacement of the friction interface. As aforementioned, for the example slotted-bolted friction-based structural component in a seismic event, the friction shims are expected to slide against the sliding plate and remain relatively static to the clamping plates. Therefore, the cumulative displacement of the friction interface between the friction shim and the sliding plate is larger than the cumulative displacement of the friction interface between the friction shim and the clamping plate. Because of the break-in effect as illustrated in Fig. 3(b), as the cumulative displacement increases, the coefficient of friction between the friction shims and the sliding plate μ_2 will become larger than the coefficient of friction between the friction shims and the clamping plates μ_1. Fig. 3(c) shows the load path of the example slotted-bolted friction-based structural component considering the break-in effect. The difference between the friction forces on top and bottom surfaces of the friction shim is balanced by the bearing action between the structural bolts and the friction shim. The magnitude of the bearing force can be computed as:

$$f_{bearing} = \mu_2 N - \mu_1 N = N(\mu_2 - \mu_1) \quad (1)$$

If the friction shims were not designed against the bearing action, the bearing action could result in elongation of the bolt hole or net section tensile failure of the friction shims as observed in [1,24,27,30]. Even though the damage due to the bearing action could be prevented by using thicker friction shims [1] or by modifying the configuration of the friction-based component [22,26,28], it is still important to characterize the tensile and bearing strengths of the composite materials so that the bearing action could be designed against.

1.2.2. Loss of preload due to material creep

When a friction-based structural component is at rest, the loss of preload is mainly attributed to the creep-induced through-thickness deformation of clamped parts. The loss of preload could induce a reduction in the friction force that a friction-based structural component could generate and therefore, should be assessed. Past relaxation tests of bolted joints [32,33] showed that compared with metallic bolted joints (steel or aluminum), composite bolted joints exhibited an increased percentage of bolt load loss over time, and this was attributed to the fact that the viscoelastic characteristics of composite materials exacerbated the creep behavior of the material in the through-thickness direction and resulted in increased through-thickness deformation. Although the loss of preload due to material creep is an important phenomenon for friction-based structural components with composite-metallic friction interfaces, it has barely been investigated in past studies listed in Section 1.1.2. Tsampras et al. [1] put the friction-based structural component used in their study with the composite (Gatke 398) to low-carbon structural steel friction interface at rest for 11 months and retested the component. A 15% loss of the sliding force was observed and the loss of the sliding force was attributed to loss of bolt pretension due to the creep-induced through-thickness deformation of clamped parts. Tsampras et al. [1] also retightened the bolts that provided the normal load to the original target normal load level and the sliding force of the component after bolt retightening was similar to the original target sliding force. For characterization and selection of composite materials for composite-metallic friction interfaces for friction-based structural components, relaxation tests are required to assess the through-thickness creep behavior of the composite material. Composite materials that would induce excessive loss of preload due to their through-thickness creep behavior should not be recommended for use in composite-metallic friction interfaces for friction-based structural components.

1.3. Scope of study

The objective of this study is to provide practical recommendations on what composite to low-carbon structural steel friction interfaces

are appropriate for earthquake structural engineering applications. Six types of phenolic-resin-based fiber-reinforced composite materials were selected for this study. A systematic testing program was proposed. Compared with past studies listed in Section 1.1.2, the testing program proposed in this study not only assessed the tribological properties of the composite-metallic friction interface through a strategically designed loading protocol, but also assessed the mechanical properties and long-term creep behavior of the composite materials, of which the discussions were limited in past studies. The proposed testing program is as follows:

- Coupon tensile tests and plate bearing tests were conducted to characterize the tensile and bearing strengths of the materials, so that the bearing action from pretensioned structural bolts as discussed in Section 1.2.1 could be designed against.
- Bolt relaxation tests were conducted to assess the through-thickness creep behavior of the composite materials so that the loss of preload due to material creep as discussed in Section 1.2.2 could be predicted.
- Friction tests of the composite-metallic friction interface were conducted. The friction test included the following testing parameters that were considered important for earthquake structural engineering applications: the normal load level, loading frequencies, sliding velocities, velocity profiles (earthquake vs. sinusoidal vs. linear), and sliding histories (the cumulative displacement, the dwell time, and previous sliding events). The ranges of testing parameters were strategically designed to reflect the working condition of a friction-based structural component in a seismic event.

2. Composite friction materials

Composite friction materials are composite materials developed for use in friction interfaces, designed to provide controlled friction forces in tribological applications. A brief discussion on the constituents, the manufacturing process, and the testing of composite friction materials is provided in this section to facilitate discussions in follow-up sections.

2.1. Constituents

According to Cox [34], the constituents of composite friction materials can be characterized into four categories:

- **Binder** is the matrix of the composite friction material. It helps to hold the constituents of the composite materials together. Commonly used binders for composite friction materials include phenolic resin and modified phenolic resin.
- **Fibers** are used in composite friction materials for enhancing mechanical strengths of the material. Besides working as structural reinforcement, fibers also significantly influence the tribological properties of composite friction materials [34]. Commonly used types of fibers for composite friction materials include organic fibers (such as cotton fibers or aramid fibers), inorganic fibers (such as glass fibers), and metallic fibers (such as brass fibers).
- **Friction modifiers** are added to adjust the coefficient of friction and wear rates of composite friction materials. They can be sub-characterized into two categories: abrasives and lubricants. Abrasives increase the coefficient of friction and the wear rate. Typically, hard materials such as metal oxides and silicates (for example, yellow iron oxide Fe_2O_3, green chromium oxide Cr_2O_3, or aluminum oxide Al_2O_3) are used as abrasives. In contrast, lubricants are used to reduce the coefficient of friction, maintain the coefficient of friction at different working temperatures, and control the wear rate. Commonly used lubricants include graphites, Teflon, and metal sulfides such as molybdenum disulfide MoS_2.
- **Filler** materials are low-cost materials added to occupy the space, lower the material cost, and sometimes modify certain material properties [35]. Fillers can be organic, inorganic, or metallic. Commonly used fillers include wollastonite, vermiculite, mica, and barite.

2.2. Manufacturing

Compression molding was used to manufacture the materials used in this study. Typically, compression molding manufacturing techniques involve three main steps: mixing, molding, and post-curing [35]. These steps can be adapted by manufacturers based on the specific raw material constituents and production requirements. This section provides an introduction of the molding process as essential background information for follow-up sections. A more detailed discussion about the manufacturing of composite friction materials is included in [34–36].

During the molding step, the mix of constituents is put into a mold closure in which it will be compressed under a certain pressure, at a certain temperature, and for a certain period. The molding pressure, temperature, and period are defined by the manufacturer. There are three types of molding closure: flash mold, semi-positive mold, and fully-positive mold. The flash mold is the simplest and least expensive to use. In the flash molding process, resin is overcharged into the mold and during molding, the overcharged resin will flow out of the mold from the edge. The product of flash molding could have inconsistent density due to overflow of overcharged resin [34,37]. The semi-positive mold allows for a less amount of overcharged resin, but the cost of the mold is higher than the flash mold. The fully-positive mold utilizes an exact metering of the mix of material constituents and provides the best density control, but the tooling cost is the highest among the three methods [34,37]. The materials tested in this study were manufactured using a flash mold. The detailed manufacturing process for the materials tested in this study is described in Section 3.1.

2.3. Testing

Standards for testing composite friction materials have been developed primarily for automotive and other industrial applications. These tests typically assess physical properties (e.g., hardness), mechanical properties (e.g., compressibility), chemical properties (e.g., working pH range), and tribological properties, reflecting the working conditions of composite friction materials in automotive applications. The tribological properties of composite friction materials for automotive applications are characterized using testing methods and equipment (e.g., Chase machines [38], FAST machines, Krauss machines, and dynamometers) that simulate braking conditions through controlled rotational motion and contact between the composite friction material and a back plate (typically cast iron). However, the existing testing methods and equipment might not be suitable for characterizing composite friction material properties for earthquake structural engineering applications, due to fundamental differences in simulated loading conditions and failure mechanisms. These differences further emphasize the need for a systematic testing program specifically designed for characterizing composite friction materials for earthquake structural engineering applications. This study addresses this need and proposes a testing program that includes coupon tensile tests, plate bearing tests, bolt relaxation tests, and friction tests, to characterize composite friction materials for use in friction-based structural components for earthquake structural engineering applications.

3. Experimental testing: Background and setup

3.1. Material overview

Six types of composite friction materials from the Gatke Series [39] manufactured and supplied by ScanPac Mfg., Inc. were tested in this

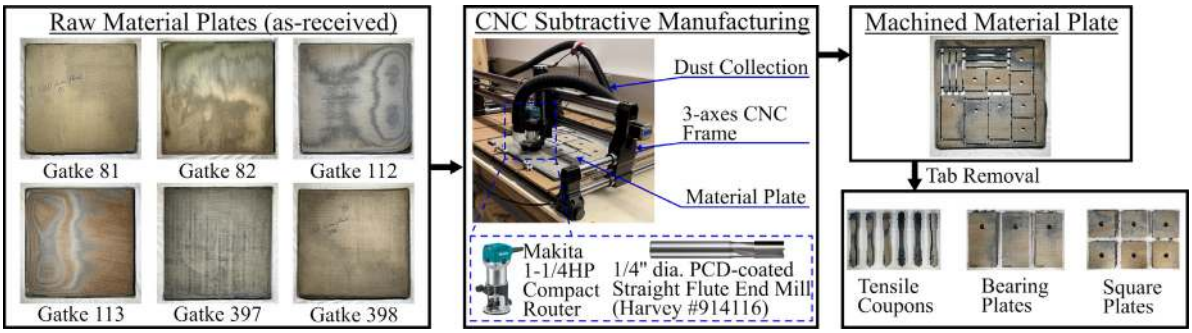


Fig. 4. Specimen preparation process.

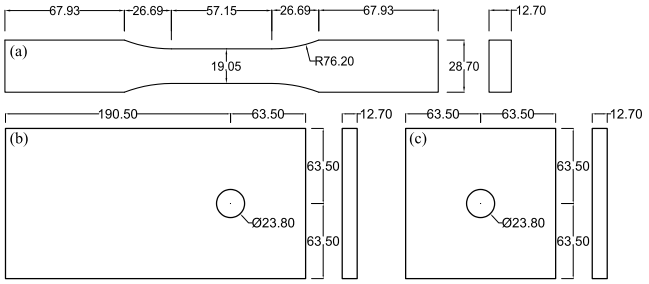


Fig. 5. Nominal dimensions of test specimens: (a) Tensile coupons (b) Bearing plates and (c) Square plates (Units: in mm).

study. Their names and constituents are shown below. In the material constituents, reinforcing fibers and the binder are listed for all the materials. Friction modifiers are listed only if they are used. Fillers are not listed.

- **Gatke 81** consists of aramid fibers, glass fibers, brass fibers, and acrylic fibers as the reinforcing fibers; yellow iron oxide, green chromium (III) oxide, and aluminum oxide as the friction modifier; and phenolic resin as the binder.
- **Gatke 82** consists of E-glass cloth as the reinforcing fibers; yellow iron oxide, green chromium (III) oxide, and aluminum oxide as the friction modifier; and phenolic resin as the binder.
- **Gatke 112** consists of cotton cloth as the reinforcing fibers; and phenolic resin as the binder.
- **Gatke 113** consists of cotton cloth as the reinforcing fibers; graphite, Teflon, and molybdenum disulfide (MoS_2) as the friction modifier; and phenolic resin as the binder.
- **Gatke 397** consists of E-glass cloth as the reinforcing fibers; and phenolic resin as the binder.
- **Gatke 398** consists of E-glass cloth as the reinforcing fibers; graphite, Teflon, and molybdenum disulfide (MoS_2) as the friction modifier; and phenolic resin as the binder.

The manufacturing process of the Gatke series materials used in this study is as follows: First, single-ply fiber cloths were impregnated with the phenolic resin mixture. After drying, the impregnated fiber cloths were cut to the required size and were compression molded using the flash mold at a temperature of 148.9 °C (300 °F) and under a pressure of 3.45 MPa (500 psi). The desired thickness of the molded plate was achieved by stacking the required number of single layers of impregnated fiber cloths and molding.

3.2. Specimen preparation

Fig. 4 shows the preparation process of the test specimens. The materials were received from the manufacturer in square plates with a nominal area of 0.61 × 0.61 m^2 (2 × 2 ft^2) and a nominal thickness of 12.7 mm (0.5 inch). A dry Computer Numerical Controlled (CNC) subtractive manufacturing approach was used in this study for machining the test specimens. A 6.35 mm ($\frac{1}{4}$ inch) diameter Polycrystalline Diamond (PCD) coated straight flute end mill (Tool #914116, Harvey Tool [40], USA) was used as the cutting tool and was installed on an 1-$\frac{1}{4}$ horsepower compact router (Makita [41], USA) for machining purposes. The cutting parameters used were: spindle speed = 10,000 RPM, resulting in a surface speed of 3.325 m/s (654.5 ft/min); cutting feed rate = 1524 mm/min (60 inch/min), resulting in a chip load of 0.0381 mm per tooth (0.0015 inch per tooth); the cutting depth was 1.27 mm (0.05 inch) per pass. No delamination or damage of the specimens was observed during machining. Tabs were used to keep the specimens in place throughout the machining process and were removed after the machining was completed. Nominal dimensions of test specimens are shown in Fig. 5.

3.3. Experimental testing set-up

3.3.1. Coupon tensile test

Fig. 6 shows the experimental testing setup of the coupon tensile test. The coupon tensile test followed ASTM D638-22 (*Test Method for Tensile Properties of Plastics*) [42]. As shown in Fig. 4, tensile coupon specimens were sampled in two orthogonal directions, i.e., 0° and 90°. These two directions were selected because they corresponded to the warp and weft directions [43] of the fiber cloth constituents. For each material, three coupons were sampled in each direction. The dimension of the tensile coupon specimen followed the Type III specimen as defined in Fig. 1 of ASTM D638-22, which is suitable for materials having a thickness from 7 to 14 mm (0.28 to 0.55 inch). Fig. 5(a) shows the nominal dimensions of the tensile coupon specimens. The total length of the specimen was 246.4 mm (9.7 inch). The total width of the specimen was 28.7 mm (1.13 inch). A narrowed section with a width of 19.05 mm (0.75 inch) was created in the middle of the specimen and the length of the narrowed part was 57.15 mm (2.25 inch). A gage length of 50.8 mm (2 inches) at the center of the narrowed part was used for computing the engineering strain. The testing machine was an MTS 810 Material Test System (MTS Systems [44], USA). The Digital Image Correlation (DIC) technique was used in the coupon tensile test to collect full-field displacement and strain data on the tensile coupon specimen throughout the test. To facilitate DIC data collection, white paint was sprayed over the specimen and a black speckle pattern was applied. The tensile test was monotonic and displacement-controlled. The speed of testing was 5.08 mm/min (0.2 inch/min), resulting in a nominal strain rate of 0.1 (mm/mm)/min at the start of the test.

3.3.2. Plate bearing test

Fig. 7 shows the experimental testing setup of the plate bearing test. The plate bearing test used ASTM D5961/D5961M-23 (*Standard Test Method for Bearing Response of Polymer Matrix Composite Laminates*) [45] Procedure A (Double Shear, Tension) as a reference, and

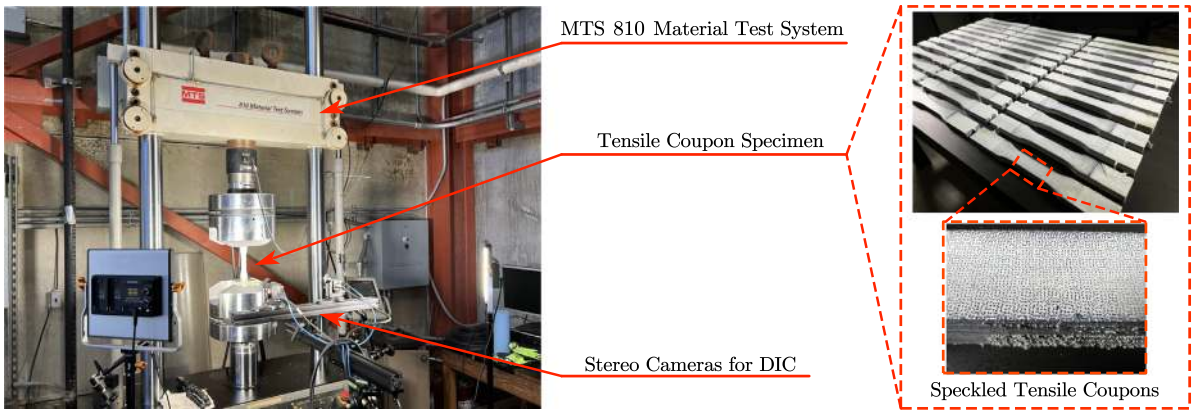


Fig. 6. Coupon tensile test setup.

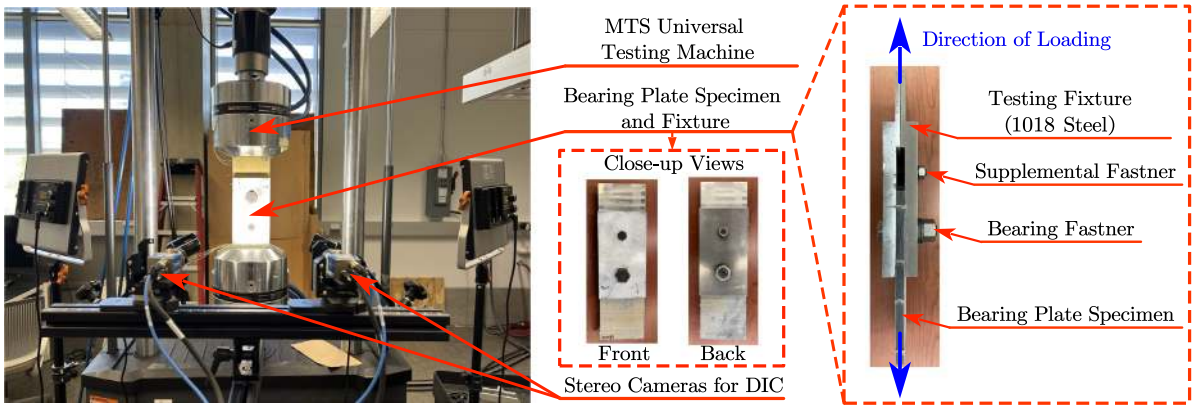


Fig. 7. Plate bearing test setup.

adjustment was made to make the test setup reflect the dimension of a sub-assembly of a full-scale slotted-bolted friction-based structural component. For each material, three specimens were tested. The plate bearing test specimen was a rectangular plate. The nominal dimension of the specimen was 254 mm × 127 mm × 12.7 mm (length(l) × width(w) × thickness(h), 10 inch × 5 inch × 0.5 inch), as shown in Fig. 5(b). A bolt hole of diameter D = 23.8 mm (15/16 inch) was created along the center line perpendicular to the width of the plate in the through-thickness direction. The diameter of the bolt hole was defined per AISC Steel Construction Manual [46] for a 22.2 mm (7/8 inch) diameter bolt with standard tolerance. The bearing fastener in this test was a 22.2 mm (7/8 inch) diameter ASTM A325 medium-strength steel heavy hex head bolt for structural applications. The nominal tensile strength of the bearing fastener was 827.4 MPa (120 ksi). The bearing load was applied through the bearing action between the bearing fastener and the plate specimen and acted perpendicular to the width of the plate. The nominal distance between the center of the bolt hole to the specimen end was e = 63.5 mm (2.5 inch), resulting in a nominal edge distance ratio (e/D) = 2.67. The nominal width to diameter ratio (w/D) was 5.33 and the nominal diameter to thickness ratio (D/h) was 1.875. In this test, a set of testing fixtures made of AISI 1018 cold-rolled steel was fabricated. The configuration of the fixture resembled a double-shear clevis. The dimensions of the fixture were designed to fulfill the strength and stiffness requirements of the test. Speckle patterns were applied on the testing fixtures and the DIC technique was used to collect full-field displacement and strain data on the bearing test fixture so that the fixture deformation throughout the test could be computed. In addition to aforementioned components, a 12.7 mm (1/2 inch) diameter ASTM A325 structural bolt was used as the supplemental fastener to assist in the assembly of the test setup.

In this test, a minimal clamping torque, just enough to stabilize the test assembly, was applied to the bearing fastener. As summarized in [47], an increase in the clamping torque will overall increase the ultimate bearing strength of the composite material because the onset of delamination is suppressed by the initial clamping pressure, and this makes the failure mode more progressive. As aforementioned, in this test, a minimal clamping torque was applied to the bearing fastener. Therefore, the experimental ultimate bearing strength computed from this test could be regarded as a lower-bound ultimate bearing strength of the material and can be used as a conservative value for practical design purposes. The plate bearing test was conducted on an MTS 370.25 servo-hydraulic load frame (MTS Systems [44], USA). Same as the coupon tensile test, the plate bearing test was also monotonic and displacement-controlled. As suggested in [45], the speed of testing was 1.27 mm/min (0.05 inch/min). The specimen was loaded until the load was equal to 70% of the maximum load recorded during the test.

3.3.3. Bolt relaxation test

Fig. 8(a) and (b) show the schematic representation and the actual test setup of the bolt relaxation test, respectively. The specimens of the bolt relaxation test were square plates having a nominal dimension of 127 mm × 127 mm × 12.7 mm (length(l) × width(w) × thickness(h), 5 inch × 5 inch × 0.5 inch), as shown in Fig. 5(c). A bolt hole of diameter D = 23.8 mm (15/16 inch) was created at the center of the plate specimen in the through-thickness direction. The diameter of the bolt hole was defined per AISC Steel Construction Manual [46] for a 22.2 mm (7/8 inch) diameter bolt with standard tolerance. The dimensions of the plate specimen and the bolt hole reflected the dimension of a sub-assembly of a friction shim for a full-scale slotted-bolted friction-based structural component. The plate specimen was clamped between

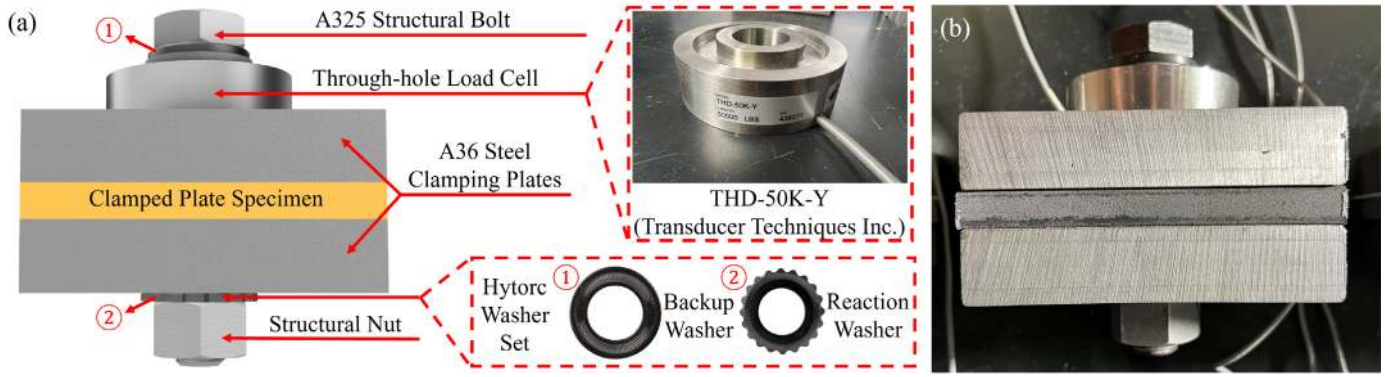


Fig. 8. Bole relaxation test: (a) schematic representation of the test setup and (b) photo of the actual test setup.

two clamping plates made of A36 steel. The clamping plates had a nominal dimension of 127 mm × 127 mm × 25.4 mm (5 inch × 5 inch × 1 inch). A bolt hole of diameter equal to 25.4 mm (1 inch) was drilled at the center of each clamping plate in the through-thickness direction. A 22.2 mm (7/8 inch) diameter ASTM A325 structural bolt was used to clamp the plates together, with a structural nut and a set of Hytorc washers (Hytorc [48], USA) including one backup washer and one reaction washer. The use of Hytorc washers eliminated the use of reaction arms or backup wrenches and hence assisted in the bolt tightening process. The Hytorc washers were manufactured in accordance with the requirements in the ASTM F3394/F3394M standard [49] and could be considered as equivalent to flat washers for structural applications. Two levels of clamping loads, i.e., high and low bolt loads, were considered in this test. The target high bolt load was 173.5 kN (39 kips), representing the minimum pretension of a 22.2 mm (7/8 inch) diameter ASTM A325 structural bolt as defined by the AISC Steel Construction Manual [46]; the target low bolt load was 57.8 kN (13 kips), representing one-third of the target high bolt load. Target high and low bolt loads resulted in target nominal normal pressure of 11 MPa (1.6 ksi) and 3.7 MPa (0.53 ksi) acting on the clamped plate specimen in the through-thickness direction, respectively. In all the tests, the threaded part of the structural bolt was lubricated using bolt anti-seize lubricants (Bostik Never-Seez regular-grade lubricants, Bostik [50], USA). The bolt loads were applied by an electric torque wrench (LST-1200, Hytorc [48], USA). The actual applied bolt load varied from the target bolt load and a variation of ±10% was considered acceptable to account for imperfection in assembly and torquing. A through-hole load cell (THD-50K-Y, Transducer Technique Inc. [51], USA) was used to monitor the bolt load throughout the testing period. The data collection frequency was set to be one data point per every 30 seconds. Data recording was stopped when a steady state of the bolt load, defined as when the bolt load loss rate was lower than or equal to -5×10^{-6} kN/s, was observed. For each material under each bolt load level, three specimens were tested. In addition to the composite plates, three A36 steel plate specimens were tested under the high bolt load to establish the baseline test cases. For selected cases as shown in Section 4.3, the pressure measurement film (Prescale® pressure measurement film, Fujifilm [52], Japan) was put between the clamped plate specimen and the clamping plates to examine the normal pressure distribution pattern around the bolt hole. The bolt relaxation test was conducted in a controlled laboratory environment. Humidity and temperature levels were measured by a humidity and temperature meter and were continuously monitored. The humidity level was about 45%~50% and the temperature was about 22.5 °C~23.5 °C throughout the test.

3.3.4. Friction test

Fig. 9(a) and (b) show schematic representations of the exploded view and the assembly of the friction test setup, respectively. Fig. 10(a) shows the photo of components of the friction test setup assembly. Fig. 10(b) shows the friction test setup assembly on the testing machine. The testing machine was an MTS 370.25 servo-hydraulic load frame, same as the bearing test. The friction test setup resembled a slotted-bolted friction-based structural component. Two ends of the friction test setup assembly were termed the fixed end and the sliding end. On the fixed end, six 22.2 mm (7/8 inch) diameter ASTM A325 structural bolts were used to clamp two steel channels and three connection plates together. Washers and nuts for structural applications were used associated with the bolts. Bolt holes with standard tolerance per AISC Steel Construction Manual were created on the steel channels and connection plates to allow the bolts to pass through. The connection plates and steel channels were made of A36 steel. The channels were commercially available C10 × 15.3 hot-rolled steel channels, of which the dimensions followed AISC Steel Construction Manual. The length of each channel was 685.8 mm (27 inch). For each bolt on the fixed end, a torque of 556 Newton·meter (410 pound·foot) was applied to tighten the bolt. The bolts on the fixed end were retightened every day before the test started to make sure that relative movement did not occur between the components on the fixed end.

Friction shims used in the friction test had the same configuration and dimensions as the clamped plate specimens in the bolt relaxation test. The nominal dimensions of the friction shims are shown in Fig. 5(c). For each steel channel, a rectangular-shaped opening was created on the channel, in which the friction shim was hosted. Sliding occurred on the end where friction shims were hosted, termed the sliding end. On the sliding end, an internal plate made of A36 steel was fabricated for testing purposes. A slot was created on the internal plate to allow for the movement of the bolt. Two recesses were created on the internal plate, in which the sliding plates were hosted. The design with recesses on the internal plate allowed for the replacement of sliding plates if needed. In this test, the sliding plates were made of low-carbon structural steel (A36 steel) and had a nominal dimension of 254 mm × 127 mm × 12.7 mm (10 inch × 5 inch × 0.5 inch). The surfaces of the A36 steel sliding plates were not specially treated. For each sliding plate, a slot was created on the plate to allow for the movement of the bolt. The friction shims made of composite friction materials were in contact with the A36 steel sliding plates and formed the friction interfaces. Loose clamping plates made of A36 steel were used to clamp the friction shims, sliding plates, and the internal plate together. A 22.2 mm (7/8 inch) diameter ASTM A325 structural bolts was used for clamping and applying the normal load to the friction interface, associated with the Hytorc washer set including one Hytorc backup washer and one Hytorc reaction washer. A through-hole load cell (THD-50K-Y from Transducer Technique Inc.) was used to monitor the bolt load throughout the friction test. During the test, the components on the fixed end, i.e., steel connection plates, bolts, washers, nuts, and two steel channels, were expected to remain static relative to each other. As the friction shim was hosted inside the rectangular-shaped opening of

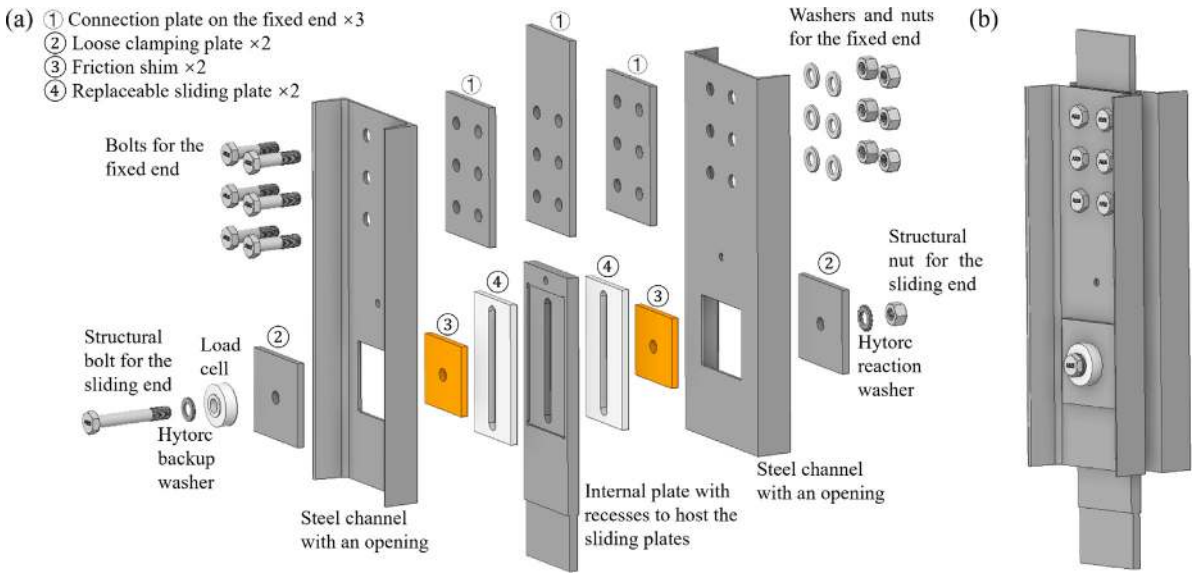


Fig. 9. Schematic representation of the friction test setup: (a) Exploded view (b) Assembly.



Fig. 10. Photos of the friction test setup: (a) Components (b) Assembly on the testing machine.

the steel channel, when the steel channels started moving relative to the internal plate, the steel channels made contact with the edge of the friction shims and pushed the friction shims to move relative to the sliding plates and to activate the sliding friction mechanism.

Similar to the bolt relaxation test, two levels of target normal loads (termed N_{target}), i.e., target high and low bolt loads, were considered in the friction test. The target high bolt load was 173.5 kN (39 kips), representing the minimum pretension of a 22.2 mm (7/8 inch) diameter ASTM A325 structural bolt as defined by the AISC Steel Construction Manual [46]; the target low bolt load was 57.8 kN (13 kips), representing one-third of the high bolt load, which considered the application of a friction-based structural component for a representative lower force demand. Target high and low bolt loads resulted in target nominal normal pressure of 13.2 MPa (1.92 ksi) and 4.4 MPa (0.64 ksi) acting on the friction interface, respectively. An exception was applied to the testing of Gatke 397, in which to prevent exceeding the testing machine's force capacity, the target high bolt load was reduced from 173.5 kN (39 kips) to 138 kN (31 kips), resulting in a nominal normal pressure of 10.5 MPa (1.53 ksi). In the friction test, the combination of one composite friction material mating with A36 steel sliding plates under one normal load level was termed one test group. The test groups were named based on the friction material used and the target normal load level (Low (L) or High (H)). For example, Test Group Gatke 81 (L) represents the test group using the composite friction material Gatke 81 and under low normal load. Six types of composite friction materials combined with two normal load levels resulted in twelve test groups. A summary of test groups of the friction test is presented in Table 1. For each test group, a pair of unworn friction shim surfaces was used to establish the friction interfaces with A36 steel sliding plates. For each material, tests for the low normal load test group were conducted first; after the tests for the low normal load test group were completed, the pair of friction shims were flipped so that the unworn surfaces on the other side of the friction shims could be used for the tests for the high normal load test group. The structural bolt on the sliding end was reused after the tests for the low normal load test group and was replaced with a new bolt after the tests for the high normal load test group, since the structural bolt yielded under a bolt load of the minimum pretension of the bolt. After completing one test group, sliding plates were removed from the test setup for inspection and cleaning. Aerosol brake parts cleaner was used with heavy-duty shop towels to clean the sliding plates to make sure that the sliding plates were free of friction dust before the start of the next test group.

A loading protocol was designed for the friction test. For each test group, twenty displacement-controlled tests (Test IDs 1~20) were conducted. Table 2 summarizes the characteristics of each test, including the type of input excitation, maximum sliding amplitude, peak

Table 1
Summary of test groups for the friction test.

Test group ID	Friction material	Target bolt load [kN]	Target nominal normal pressure [MPa]
Gatke 81 (L)	Gatke 81	57.8	4.4
Gatke 81 (H)		173.5	13.2
Gatke 82 (L)	Gatke 82	57.8	4.4
Gatke 82 (H)		173.5	13.2
Gatke 112 (L)	Gatke 112	57.8	4.4
Gatke 112 (H)		173.5	13.2
Gatke 113 (L)	Gatke 113	57.8	4.4
Gatke 113 (H)		173.5	13.2
Gatke 397 (L)	Gatke 397	57.8	4.4
Gatke 397 (H)		138	10.5
Gatke 398 (L)	Gatke 398	57.8	4.4
Gatke 398 (H)		173.5	13.2

sliding velocity, loading frequency, cumulative displacement, duration, dwell time, and the descriptions of each test. For Test ID i, dwell time is defined as the idle time between Test IDs i and i + 1. Fig. 11 shows the displacement histories of the input excitation, the cumulative displacement history of each test, and the history of absolute sliding velocities of each test. For the loading protocol, Test IDs 1~3 were three break-in tests, termed Brk1~3 as shown in Fig. 11. The break-in tests were designed to establish and assess the break-in effect of the friction interface. The break-in tests had ramped sinusoidal waves as the displacement histories of the input excitation. A maximum displacement amplitude of 50.8 mm (2 inches) and a peak sliding velocity of 12.7 mm/s (0.5 inch/s) were imposed. After each break-in test, the bolt on the sliding end that provided normal load to the friction interface was retightened to the target bolt load level as at the beginning of the test, if bolt load loss was observed. The dwell time of Test IDs 1~3 depended on the retightening practice and thus was varying. Test ID 4 assessed the response of the friction interface given an earthquake-type input excitation. The displacement history of the earthquake-type input excitation was a representative response of a friction-based structural component from numerical earthquake simulations. The sliding velocity imposed by the representative displacement response was scaled down by elongating the testing period so that it could be limited below the testing machine's capacity. A detailed discussion of the numerical earthquake simulation is beyond the scope of this study and thus not included in this paper. Test IDs 5~10 were six tests having ramped sinusoidal waves as the displacement histories of the input excitation, with different peak sliding velocities to assess how sliding velocities would affect the response of the friction interface. Three levels of peak sliding velocities were assessed in Test IDs 5~10. Test IDs 5 and 10 had a peak sliding velocity of 12.7 mm/s (0.5 inch/s); Test IDs 6 and 9 had a peak sliding velocity of 25.4 mm/s (1.0 inch/s); Test IDs 7 and 8 had a peak sliding velocity of 63.5 mm/s (2.5 inch/s). The peak sliding velocities were determined based on the testing machine's capacity, and were justified using the numerical analysis results reported in [53]. Test IDs 5~10 each had a cumulative displacement of 514 mm (20.2 inches) and the value of the cumulative displacement was also justified using the numerical analysis results reported in [53]. Test ID 11 had the same imposed displacement history as Test ID 4 and was designed to assess the repeatability of the response of the friction interface given an earthquake-type input excitation. Test IDs 12~13 were two tests having ramped linear waves as the displacement histories of the input excitation with a peak sliding velocity of 25.4 mm/s (1.0 inch/s), equal to that of Test IDs 6 and 9. The difference between ramped sinusoidal waves and ramped linear waves was that for ramped linear waves, the anticipated absolute sliding velocity remained constant throughout the test while for ramped sinusoidal waves, the anticipated absolute sliding velocity varied. In addition, compared with Test IDs 6 and 9, Test IDs 12~13 had a larger loading frequency. Following Test IDs 12~13 and similar to Test ID 11, Test ID 14 had the same imposed displacement history as Test ID 4 and was designed to assess the repeatability of the response of the friction interface given an earthquake-type input excitation. For Test IDs 4~14, the dwell time between two consecutive tests was ten seconds. Test IDs 15~20 assessed the effect of dwell time on the response of the friction interface. The assessment method was that a ramped sinusoidal wave with a peak sliding velocity of 63.5 mm/s (2.5 inch/s) was firstly run. This test was termed the prior test of the dwell time effect assessment. After the prior test, the test setup was held idle for a predefined amount of dwell time. Afterward, an earthquake-type input excitation was run to evaluate how the coefficient of friction changed after this certain amount of dwell time. This step was termed the posterior test of the dwell time effect assessment. Test IDs 15, 17, and 19 were three prior tests and Test IDs 16, 18, and 20 were three corresponding posterior tests. Three different dwell times were assessed. Between Test IDs 15 and 16, the dwell time was 10 seconds; between Test IDs 17 and 18, the dwell time was 10 minutes; between Test IDs 19 and 20, the dwell time was 30 minutes. In Fig. 11, they are marked as DT10s, DT10m, and DT30m respectively. Twenty tests resulted in a total cumulative displacement of 14.407 meters which is effectively equal to the cumulative sliding of the friction interface.

In the friction test, recorded data included the connection force, the connection displacement, and the bolt load of the structural bolt on the sliding end. Data collection of three quantities was synchronized.

3.4. Digital image correlation technique

A Digital Image Correlation (DIC) technique was used in the testing series to quantify full-field displacement and strain on (1) tensile coupon specimens and (2) bearing test fixtures. Utilizing the DIC technique typically consists of the following steps: (1) Specimen preparation, including spray painting the specimen and applying the speckle pattern of appropriate size over the region of interest on the specimen; (2) System assembly and camera positioning; (3) Camera focusing; (4) System calibration, in which the intrinsic parameters (e.g., focal lengths of the lenses) and extrinsic parameters (e.g., relative positioning between cameras) of the camera lenses will be determined; (5) Image collection throughout the testing; and finally, (6) Data analysis. An important characteristic of the DIC technique is the full-field nature of the measurement data, which provides the possibility to look into highly localized material behavior, for example, strain localization during the testing process [54]. Additionally, in the tensile test, the full-field measurement data enabled an accurate assessment of the engineering strain over the gauge length of the tensile coupon specimens, without using additional instruments like strain gauges or extensometers [54]. The full-field measurement data also enabled the collection of displacement-related data in the transverse direction of the tensile coupon specimens and therefore, enabled the assessment of the Poisson's ratio of the materials [54].

In the setup for this series of experimental testing, two Basler ace acA4112-30um cameras were used. The cameras used a Sony IMX253

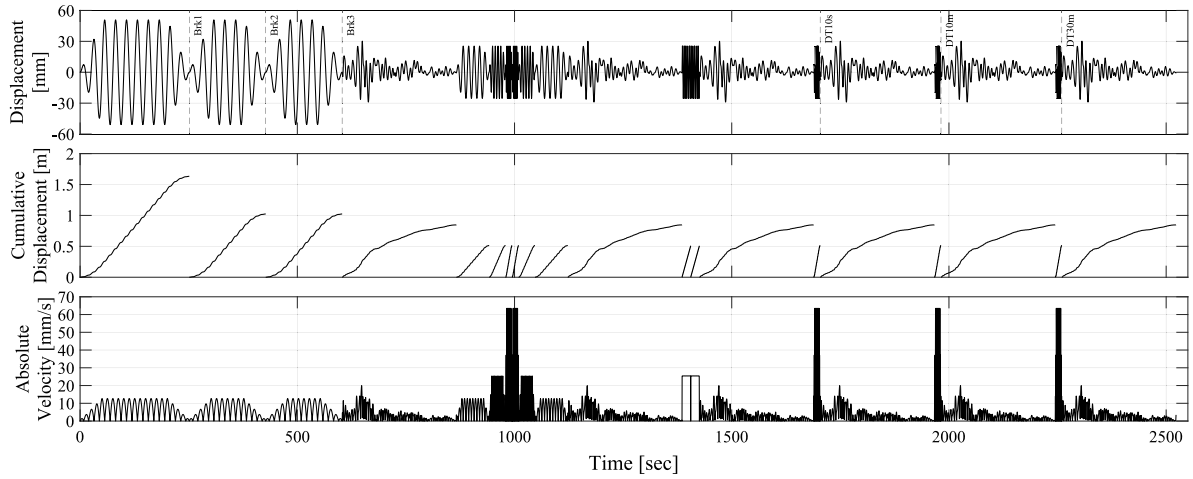


Fig. 11. Friction test loading protocol. From top to bottom: imposed displacement history (ends of break-in tests are marked as Brk1~3 and the dwell time periods for dwell time assessment tests are marked as DT10s, DT10m, and DT30m); cumulative displacement history of each test; absolute sliding velocity history.

monochrome sensor, having a resolution of 12 megapixels (4096 pixels × 3000 pixels) and a maximum frame rate of 30 frames per second (FPS). The lenses were Schneider-Kreuznach JADE 2.8/25 C lenses, which had a focal length of 25 mm and a range of f-number (the ratio of a lens's focal length to its aperture diameter) from 2.8 to 16. The commercial software, Vic-Snap (Correlated Solutions [55], USA), was used to facilitate the image collection process. In the data analysis stage, the commercial software, Vic-3D (Correlated Solutions [55], USA), was used to compute full-field displacement-related data by tracking the motions of the speckle patterns through the sequence of the test images.

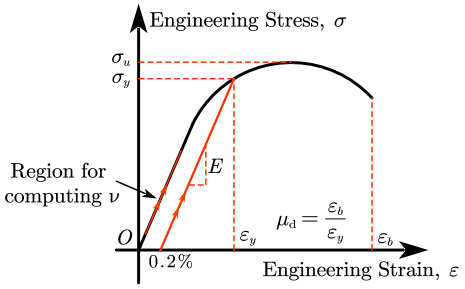


Fig. 12. Engineering parameters of interest for the coupon tensile test.

4. Results

4.1. Coupon tensile test

Fig. 12 shows a schematic representation of the expected engineering stress–strain curve of the coupon tensile test and is used to define engineering parameters of interest. Fig. 13 shows the results of the coupon tensile test. Engineering stress versus engineering strain curves upon failure of all tensile coupons are plotted. Results shown in black lines and red lines correspond to tensile coupons sampled in the warp and weft directions, respectively. According to ASTM D638, the modulus of elasticity (E) is defined as "*the ratio of stress to corresponding strain below the proportional limit of a material*". The yield strength (σ_y) is defined as "*the stress at which a material exhibits a specified limiting deviation from the proportionality of stress to strain*". In this test for all the specimens, since the stress–strain curve in the yield range was of gradual curvature change and a distinct yield point was not well-defined, 0.2% offset yield strength (the stress at which the strain exceeded 0.2% an extension of the initial proportional portion of the stress–strain curve) was considered as the yield strength of the material. The yield strain (ε_y) is defined as the strain at the intersection point between the 0.2% extension line and the stress–strain curve. The tensile strength (σ_u) is defined as "*the maximum tensile stress sustained by the specimen during the test*". The tensile strain at break (ε_b) is defined as the maximum strain that the tensile coupon specimen sustained during the test before breaking. The ductility μ_d is defined as the ratio between ε_b and ε_y. The Poisson's ratio (ν) is defined as "*the absolute value of the ratio of transverse strain to the corresponding axial strain resulting from uniformly distributed axial stress below the proportional limit of the material*". The mean material tensile properties of six materials that were tested are summarized in Table 3.

As shown in Fig. 13 and Table 3, the directionality with respect to warp and weft directions was observed in all materials except for Gatke 113. Fiber-reinforced composite laminated materials exhibit directionality because of the directionality of their constituents. Specifically, fiber cloth has a higher tensile strength in the warp direction than in the weft direction, resulting in the directionality of laminated composites with respect to strength. From Table 3, it is observed that in addition to strength, other engineering parameters, including modulus of elasticity (E), Poisson's ratio (ν), yield strain (ε_y), tensile strain at break (ε_b), and ductility (μ_d), also exhibited directionality with respect to warp and weft directions. In the case of Gatke 113, hypothetically during the manufacturing process, the orientation of the fiber cloth was not tightly controlled during the stacking process; as a result, the warp and weft directions were potentially interchanged, resulting in the loss of directionality for Gatke 113. Hypothetically, a more consistent result with respect to tensile strength could be obtained if tighter quality control were imposed on the stacking of fiber cloths during the manufacturing process.

For Gatke 112, 397, and 398, two different failure modes (i.e., tension failure and bond failure) were observed. Example photos of two Gatke 112 specimens with different failure modes are shown in Fig. 13. The different failure modes were attributed to the inhomogeneous distribution of raw material constituents from manufacturing. As discussed in Section 2.2, the flash compression molding process can produce composite material plates having inconsistent density due to overflow of overcharged resin. The seepage of overcharged resin results in regions with a lower concentration of resin than anticipated. From Gatke 112 results, it is observed that tensile coupon specimens that exhibited bond failure during the tensile test appeared to be sampled from regions with a lower concentration of resin. A lower concentration of resin led to weaker bonding between the laminates and exacerbated the delamination of the composite material. This effect consequently resulted in bond failure of the tensile coupon specimen.

Table 2
Friction test loading protocol: Imposed displacement histories.

Test ID	Input type	Maximum amplitude [mm]	Peak velocity [mm/s]	Loading frequency [Hz]	Cumulative displacement [mm]	Duration [s]	Dwell time [s]	Descriptions
1	Ramped sine	50.8	12.7	0.0398	1633	251.3	Varying	Break-in test one (Brk1) to establish and assess the break-in effect
2	Ramped sine	50.8	12.7	0.0398	1023.4	175.9	Varying	Break-in test two (Brk2) to establish and assess the break-in effect
3	Ramped sine	50.8	12.7	0.0398	1023.4	175.9	Varying	Break-in test three (Brk3) to establish and assess the break-in effect
4	Earthquake	30.1	20.0	N/A	847.6	263	10	Assess the friction interface response after the establishment of the break-in effect under earthquake-type input excitation
5	Ramped sine	25.4	12.7	0.0796	514	75.4	10	Assess the friction interface response under ramped sinusoidal motion with a peak sliding velocity of 12.7 mm/s (0.5 in./s)
6	Ramped sine	25.4	25.4	0.1592	514	37.7	10	Assess the friction interface response under ramped sinusoidal motion with a peak sliding velocity of 25.4 mm/s (1.0 in./s)
7	Ramped sine	25.4	63.5	0.3979	514	15.1	10	Assess the friction interface response under ramped sinusoidal motion with a peak sliding velocity of 63.5 mm/s (2.5 in./s)
8	Ramped sine	25.4	63.5	0.3979	514	15.1	10	Assess repeatability of the friction interface response under ramped sinusoidal motion with a peak sliding velocity of 63.5 mm/s (2.5 in./s), compared with Test ID 7
9	Ramped sine	25.4	25.4	0.1592	514	37.7	10	Assess repeatability of the friction interface response under ramped sinusoidal motion with a peak sliding velocity of 25.4 mm/s (1.0 in./s), compared with Test ID 6
10	Ramped sine	25.4	12.7	0.0796	514	75.4	10	Assess repeatability of the friction interface response under ramped sinusoidal motion with a peak sliding velocity of 12.7 mm/s (0.5 in./s), compared with Test ID 5
11	Earthquake	30.1	20.0	N/A	847.6	263	10	Assess repeatability of friction interface response under earthquake-type input excitation, compared with Test ID 4
12	Ramped linear	25.4	25.4	0.25	508	20	10	Assess the friction interface response under ramped linear motion with a peak sliding velocity same as Test IDs 6 and 7
13	Ramped linear	25.4	25.4	0.25	508	20	10	Assess repeatability of the friction interface response under ramped linear motion, compared with Test ID 12
14	Earthquake	30.1	20.0	N/A	847.6	263	10	Assess repeatability of friction interface response under earthquake-type input excitation, compared with Test IDs 4 and 11
15	Ramped sine	25.4	63.5	0.3979	514	15.1	10	Prior test of dwell time effect assessment with 10 seconds dwell time
16	Earthquake	30.1	20.0	N/A	847.6	263	10	Posterior test of dwell time effect assessment with 10 seconds dwell time
17	Ramped sine	25.4	63.5	0.3979	514	15.1	600	Prior test of dwell time effect assessment with 10 minutes dwell time
18	Earthquake	30.1	20.0	N/A	847.6	263	10	Posterior test of dwell time effect assessment with 10 minutes dwell time
19	Ramped sine	25.4	63.5	0.3979	514	15.1	1800	Prior test of dwell time effect assessment with 30 minutes dwell time
20	Earthquake	30.1	20.0	N/A	847.6	263	N/A	Posterior test of dwell time effect assessment with 30 minutes dwell time

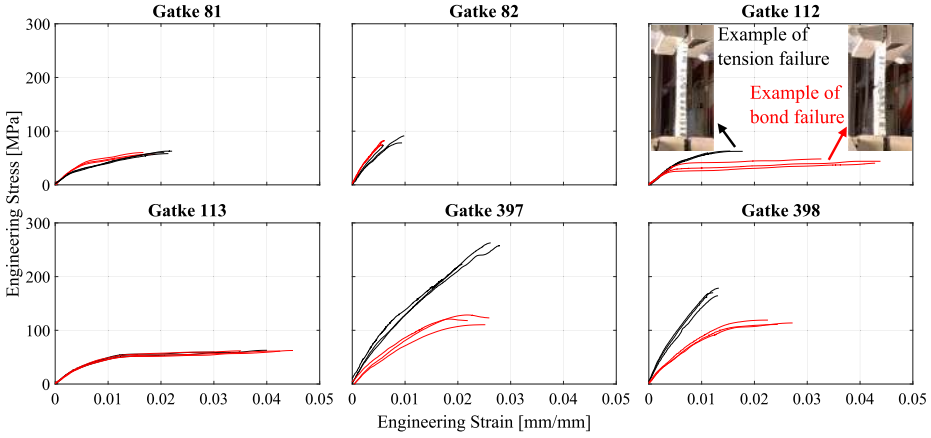


Fig. 13. Coupon tensile test results: engineering stress–strain curves upon failure (example photos of two Gatke 112 specimens with different failure modes are shown with Gatke 112 results).

Table 3
Summary of mean material tensile properties from the coupon tensile test.

Materials	Direction	Yield strength[a,b] σ_y [MPa]	Tensile strength σ_u [MPa]	Modulus of elasticity E [GPa]	Poisson's ratio ν [–]	Yield strain ε_y [mm/mm]	Tensile strain at break ε_b [mm/mm]	Ductility μ_d [–]	Primary failure mode
Gatke 81	Warp	32.71	60.34	7.26	0.20~0.25	0.0065	0.0214	3.294	Tension
	Weft	42.69	57.38	9.20	0.25~0.30	0.0068	0.0174	2.548	Tension
Gatke 82	Warp	–	81.42	14.13	0.10~0.20	–	0.0080	–	Tension
	Weft	–	79.69	18.52	0.15~0.20	–	0.0057	–	Tension
Gatke 112	Warp	47.80	61.49	8.80	0.25~0.30	0.0075	0.0148	1.978	Tension
	Weft	31.95	44.20	7.38	0.20~0.30	0.0064	0.0398	6.200	Bond
Gatke 113	N/A	38.97	61.50	7.96	0.25~0.30	0.0070	0.0386	5.506	Tension
Gatke 397	Warp	120.56	248.06	17.38	0.20~0.30	0.0090	0.0250	2.787	Tension
	Weft	64.22	119.96	11.39	0.10~0.15	0.0076	0.0244	3.192	Bond + Tension
Gatke 398	Warp	133.24	170.97	20.71	0.05~0.20	0.0085	0.0128	1.511	Tension
	Weft	68.57	114.52	12.52	0.05~0.20	0.0075	0.0247	3.302	Bond + Tension

[a] 0.2% offset yield strength was considered as the materials' yield strength.
[b] In the case of Gatke 82, the ultimate tensile strain was too small that the 0.2% offset line did not have intersection with the stress–strain curve.

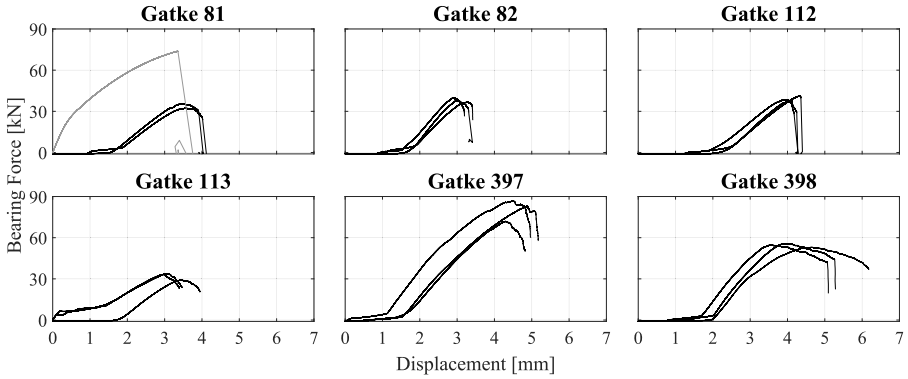


Fig. 14. Plate bearing test results: bearing force versus the recorded displacement.

4.2. Plate bearing test

Fig. 14 shows the bearing force versus the recorded displacement plots of all bearing plate specimens. In the bearing test, the bearing force started increasing once the bearing fastener was in contact with the bolt hole edge of the bearing plate specimen. The recorded displacement response consisted of three parts: bearing fastener deformation, fixture deformation, and bearing plate specimen deformation. The bearing fastener was assumed to deform elastically and the elastic deformation was considered negligible compared with the recorded displacement response. The fixture deformation was computed using the DIC technique and measured to be in the order of 0.03 mm. It was less than one percent of the recorded displacement response and therefore, the fixture deformation was also considered negligible. The recorded displacement response was considered representative of the bearing plate specimen deformation. Note that for Gatke 81, there was one test in which an excessive clamping torque was applied, resulting in a tensile failure outside the bolt hole region. This test was considered invalid and marked in gray in Fig. 14.

Table 4 summarizes the mean material bearing properties, including the mean ultimate bearing strength F^{bru} and failure modes of the specimens. Per ASTM D5961, F^{bru} is equal to:

$$F^{bru} = \frac{P_u}{kDh} \tag{2}$$

where P_u is the maximum bearing load that the specimen sustained prior to failure; k is the load-per-hole factor and is equal to one for assembly with one bearing fastener; D is the bolt hole diameter and h is the thickness of the bearing plate specimen. The formula provided by ASTM D5961 computes the material ultimate bearing strength in an average sense and does not take stress concentration into consideration. As summarized in Table 4, two failure modes, i.e., net tension and cleavage [45], were observed in the test. Pure bearing failure characterized by significant elongation of bolt holes was not observed in this test because the clamping torque applied was considered minimal and therefore, the confinement from the adjacent assembly to the bearing plate specimen was minimal, which inhibited the formation of the pure bearing failure mode.

4.3. Bolt relaxation test

Fig. 15 shows the bolt relaxation test results, in which the time history of the normalized bolt load, i.e., recorded bolt load normalized by the initial bolt load (N/N_{ini}), is plotted. Fig. 16(a) further summarizes the percentage of bolt load loss of each specimen upon reaching the steady state. As observed in Fig. 16(a), the specimens with A36 steel plates being clamped, as expected, exhibited the least percentage of bolt load loss. Except for three specimens, the specimens with composite friction material plates being clamped, regardless of the material type, exhibited a percentage of bolt load loss ranging approximately from 4.5% to 15%. In one specimen with a Gatke 81 plate being clamped under high bolt load, a 18.55% bolt load loss was observed. In one specimen with a Gatke 113 plate being clamped under low bolt load, a 26.04% bolt load loss was observed. It is noteworthy that in one specimen with a Gatke 112 plate being clamped under high bolt load as highlighted in Fig. 16(a), a 37.12% bolt load loss was observed. This outlier case of the Gatke 112 specimen was further investigated and explained in follow-up paragraphs. For Gatke 81, 112, and 398, test specimens under high bolt load overall exhibited an increased percentage of bolt load loss compared with test specimens under low

Table 4
Summary of mean ultimate bearing strengths and specimen failure modes from the plate bearing test.

Materials	Mean ultimate bearing strength F^{bru} [MPa]	Failure mode
Gatke 81	112.03	All specimens failed due to net tension
Gatke 82	126.58	All specimens failed due to cleavage
Gatke 112	129.72	All specimens failed due to net tension
Gatke 113	106.36	All specimens failed due to net tension
Gatke 397	266.53	All specimens failed due to cleavage
Gatke 398	180.06	One specimen failed due to net tension; two specimens failed due to cleavage

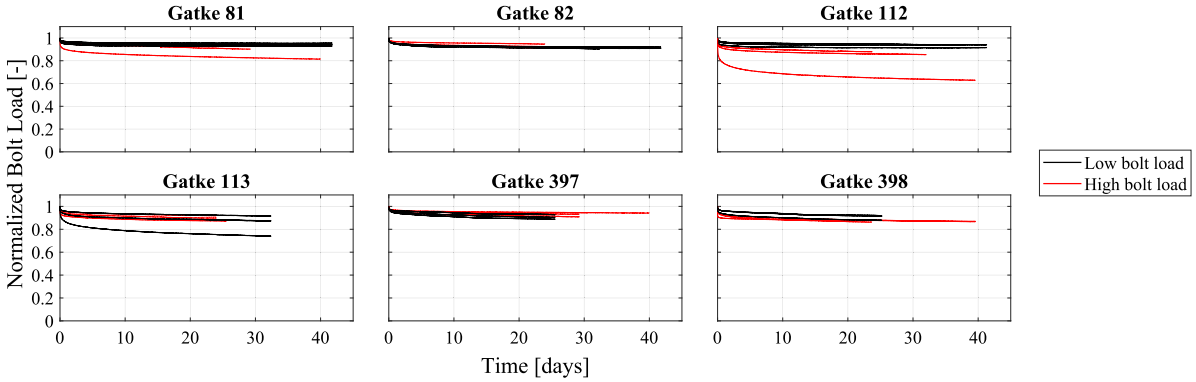


Fig. 15. Bolt relaxation test results: normalized bolt load (N/N_{ini}) time history.

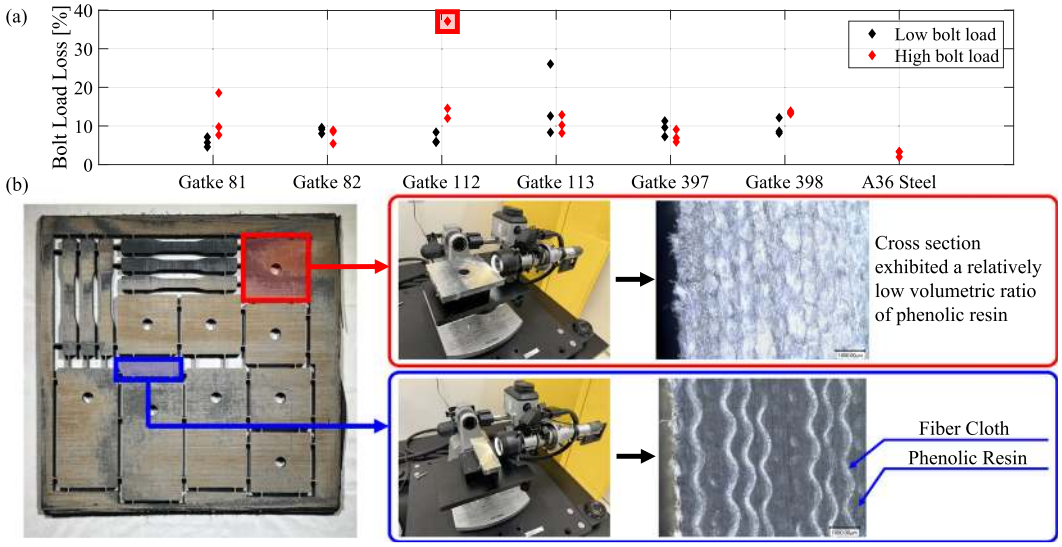


Fig. 16. (a) Bolt load loss of all test specimens upon reaching the steady state of the bolt load; one of the results of Gatke 112 specimens with the largest bolt load loss of 37.12% is highlighted (b) Microscopy images of the Gatke 112 specimen with 37.12% bolt load loss and another specimen sampled in the region with appropriate volumetric ratio of phenolic resin.

bolt load. In contrast, for Gatke 82, 113, and 397, test specimens under high bolt load overall exhibited a similar or decreased percentage of bolt load loss compared with test specimens with low bolt load. For the materials that were tested, the correlation between material constituents and the percentage of bolt load loss was insignificant.

The outlier case of the Gatke 112 specimen with a bolt load loss of 37.12% was further investigated. An optical microscope (VHX-1000, Keyence [56], USA) was adopted to examine the cross section of the specimen. Microscopy images are shown in Fig. 16(b). Compared with another rectangular specimen sampled near the center of the machined plate of which the cross sectional view exhibited a clear and well-defined laminated structure, the cross sectional view of the Gatke 112 specimen with a bolt load loss of 37.12% exhibited a relatively low volumetric ratio of phenolic resin. Although the images of the outlier Gatke 113 specimen (with a bolt load loss of 26.04% under a low bolt load) were not presented, the examination of the specimen confirmed that it had the same issue as the outlier Gatke 112 specimen, that the cross section of the outlier Gatke 113 specimen also exhibited a relatively low volumetric ratio of phenolic resin. The observed relatively low volumetric ratio of phenolic resin in the outlier specimens was attributed to the manufacturing defect. As discussed in Section 2.2, the flash molding technique could result in products having inconsistent density due to overflow of overcharged resin. From Fig. 16(b), it can be observed that the Gatke 112 specimen with a bolt load loss of 37.12% was sampled close to the edge of the material plate, where the seepage of overcharged phenolic resin happened. The overflow of overcharged phenolic resin left the region close to the edge of the material plate lack of phenolic resin and resulted in an excessive percentage of bolt load loss of the specimen. Fig. 17 shows the images of the pressure recording films of two Gatke 112 specimens from the bolt relaxation

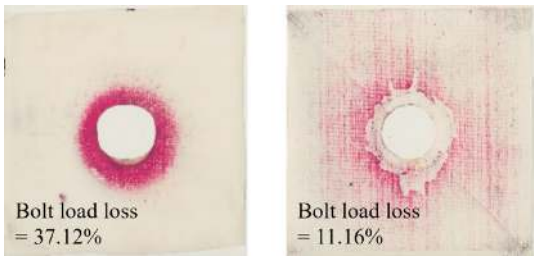


Fig. 17. Images of pressure recording films of two Gatke 112 specimens from the bolt relaxation test.

test. On the pressure recording films, pink areas represent areas that carried the normal load. Two patterns of normal pressure distribution can be observed. For the case with a bolt load loss of 37.12%, the normal pressure was concentrated around the bolt hole while for the case with a bolt load loss of 11.16%, the distribution of the normal pressure was more uniform. From the result of Gatke 112 specimens, it can be observed that the specimen with a concentrated normal pressure distribution pattern had a higher percentage of bolt load loss compared with the specimen with a more uniformly distributed normal pressure pattern. The normal pressure distribution pattern reflected the compressive stiffness of the specimen in the through-thickness direction, which was affected by the micro-structure of the composite laminates. The relatively low volumetric ratio of phenolic resin resulted in a reduced compressive stiffness of the specimen in the through-thickness direction, causing the normal pressure in the through-thickness direction to be more concentrated around the bolt hole, and consequently resulted in an excessive percentage of bolt load loss. The results of the bolt relaxation test highlighted the importance of quality control in the manufacturing process of composite friction materials for friction-based structural components.

4.4. Friction test

This section presents the results of the friction test. In this section, the conditions of friction shims and sliding plates are first shown. Within each test group, test data from different test IDs was grouped, processed, and analyzed, with an emphasis on different testing parameters and sliding mechanisms. Test IDs 1~3 were grouped to assess the break-in effect of the friction interface; Test IDs 5~10 were grouped to assess the effect of sliding velocities on the response of the friction interface; Test IDs 6, 9, 12, and 13 were grouped to assess the oscillation in friction force responses due to low-velocity stick–slip behavior; Test IDs 4, 11, and 14 were grouped to assess the response and the repeatability of the response of the friction interface under earthquake-type input excitation; Test IDs 15~20 were grouped to assess the effect of dwell time on the response of the friction interface.

4.4.1. Friction shim conditions

Fig. 18 shows the friction shim conditions before and after the friction test. For each test group, the photo on the left hand side shows the friction shim condition before the friction test, and the photo on the right hand side shows the friction shim condition after the friction test. For all of the friction shims, the surfaces that formed the friction interfaces turned black after the friction test. The black layer was a carbon-rich char structure as the product of the thermo-oxidative degradation process of the phenolic resin matrix [34].

Out of twelve test groups, friction shims from ten test groups had no damage after the friction test. One representative example is shown in Fig. 19(a). In one test group (Gatke 81 (L)), friction shims exhibited minor damage, characterized by composite materials migrating in the sliding direction under the friction force but not getting scraped off, as shown in Fig. 19(b). In this case, the friction test could still be continued toward the end of the loading protocol. In one test group (Gatke 113 (H)), friction shims exhibited severe damage during Test ID 1, characterized by a significant amount of material being scraped off and removed from the surface of the friction shim, as shown in Fig. 19(c) and (d). In this case, the friction shims were significantly thinned, inducing a drop of the bolt load by 70%. This test group was stopped prematurely after the completion of Test ID 1.

4.4.2. Sliding plates conditions

As described in Section 3.3.4, after the completion of one test group, the pair of A36 steel sliding plates was removed from the test setup for inspection and cleaning purposes. Fig. 20(a) shows the unworn state of the A36 steel sliding plates used in this study. Fig. 20(b) shows one representative example of sliding plate conditions after the completion of one test group and before cleaning, from Gatke 112 (L). Friction dust was observed to spread over the surfaces of the sliding plates. Aerosol brake parts cleaner and shop towels were used to clean the sliding plates. Fig. 20(c) shows a representative example of sliding plates conditions after cleaning. Visual inspection of the sliding plates indicated that except for some removal of the mill scale on the sliding plate surfaces, the surface topography of the sliding plates was overall unchanged; hence, the A36 steel sliding plates were reused for all test groups in this study.

4.4.3. Break-in effect assessment

According to Blau [29], the break-in process is defined as the initial sliding process when two surfaces are first brought into contact under the normal load and start sliding relative to each other, in which changes in the surface conditions occur. During the break-in process, changes in the coefficient of friction and the wear rate of a friction interface usually happened. After the break-in process, the coefficient of friction and the wear rate of a friction interface would reach a relatively constant level, and Blau [29] defined this state as the "steady state". The break-in effect is defined as the effect of the break-in process on the response of the friction interface.

Fig. 21 shows the assessment results of the break-in effect. The computed coefficient of friction (COF) $\mu_{computed}$ is defined as $\mu_{\text{computed}} = \left|\frac{f}{n_b n_s N}\right|$, where f is the recorded connection force, $n_b = 1$ is the number of bolts that provided normal force onto the friction interface, $n_s = 2$ is the number of friction interfaces that contributed to the friction force, and N is the recorded bolt load. The absolute operator is to account for the fact that the coefficient of friction μ has to be positive. In Fig. 21, each purple circular marker represents the mean $\mu_{computed}$ within one sliding travel, where the sliding travel is defined as the sliding between two consecutive points of zero sliding velocity (i.e., the sliding direction is monotonic within one sliding travel), and its corresponding mean cumulative displacement within this sliding travel. To analyze the break-in effect quantitatively, regression analysis with a Logistic function was performed for purple circular markers. The Logistic function is defined as:

$$\mu = \frac{L}{1 + e^{-k(x - x_0)}} \tag{3}$$

where μ is the coefficient of friction and x is the cumulative displacement. L, k, and x_0 are three parameters of the Logistic function to be obtained from the regression analysis. L is mathematically the maximum value of the Logistic function and physically represents the steady-state coefficient of friction of the friction interface given the Logistic function model; k and x_0 define the steepness of the function and x-value of the inflection point of the function, respectively. They do not have physical meanings in this context but assist in obtaining quantities of interest. As a standard practice, the fitness of the obtained Logistic function model from the regression analysis for the data points was quantified by the coefficient of determination, R^2 (R-squared). R^2 values of each test group are summarized in Table 5. Overall, the Logistic function had a good fit with the data points, indicated by an

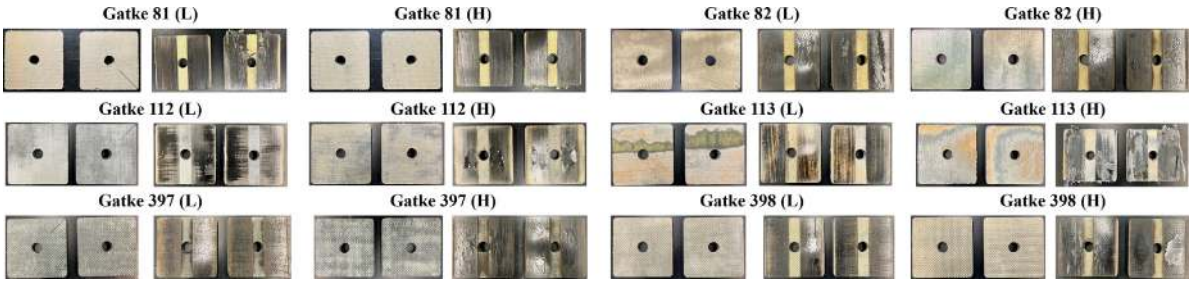


Fig. 18. Friction shims conditions before (left) and after (right) the friction test.

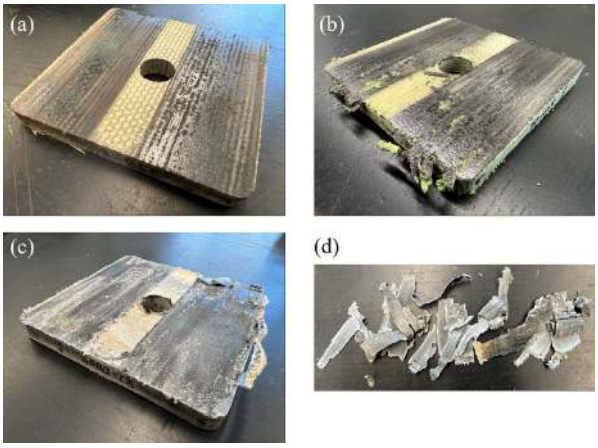


Fig. 19. Friction shims with (a) no damage (example friction shim from Test Group Gatke 398 (L)) (b) minor damage (example friction shim from Test Group Gatke 81 (L)) (c) severe damage (example friction shim from Test Group Gatke 113 (H)) and (d) materials scraped off from the friction shim surface in (c).

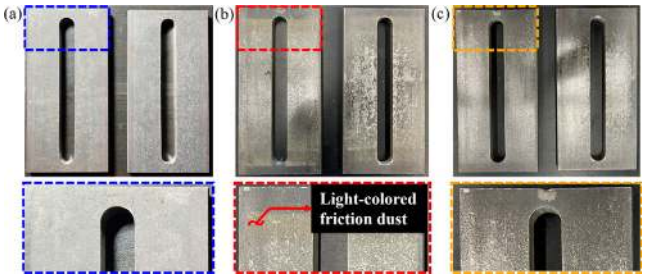


Fig. 20. (a) Unworn sliding plates before the friction test (b) Representative example of sliding plates conditions after completing one test group (Gatke 112 (L)) and before cleaning (c) Representative example of sliding plates conditions after cleaning using aerosol brake parts cleaner and heavy-duty shop towels.

R^2 value larger than 0.8. One exception was Test Group Gatke 112 (H), in which an R^2 value equal to 0.32 was obtained from the regression analysis. From Fig. 21, it is observed that for Test Group Gatke 112 (H), as the cumulative displacement increased, the coefficient of friction increased, reached a peak, and then decreased. The Logistic function could not capture the declining trend and therefore, could not fit well with the data points for Test Group Gatke 112 (H).

Except for Test Groups Gatke 112 (H) and Gatke 113 (H), the identified steady-state coefficients of friction, i.e., parameters L for the fitted Logistic function, are termed μ_{ss} and are summarized in Table 5. The mean coefficients of friction from Test ID 4 (termed $\overline{\mu_4}$) are also summarized in Table 5 and the relative difference between μ_{ss} and $\overline{\mu_4}$ is computed as $\delta_{ss\text{-}4} = \frac{\overline{\mu_4}-\mu_{ss}}{\mu_{ss}}$ and is reported in Table 5. It is noted that for all test groups, the magnitude of $\delta_{ss\text{-}4}$ was less than 10%, which proved that upon the establishment of the break-in effect, the coefficient of friction reached a relatively constant level and also, the fitted Logistic function overall captured the break-in response of the friction interfaces. The relative difference between the initial coefficients of friction from Test ID 1 (termed μ_{ini}) and μ_{ss} is computed as $\delta_{ini\text{-}ss} = \frac{\mu_{ss}-\mu_{ini}}{\mu_{ini}}$ and is also reported in Table 5.

In this study, the start of the steady state is defined as when the derivative of the fitted Logistic function, $\frac{d\mu}{dx}$, reaches 0.01. The cumulative displacements at the start of the steady state, termed the identified steady-state cumulative displacement, are summarized in Table 5 and are plotted in Fig. 21 in dashed blue lines. From Table 5 and Fig. 21, it is observed that the break-in effect depends on the material constituents of the composite friction materials and the normal load level. Cotton-fiber-reinforced composite friction materials (Gatke 112 and 113) had shorter steady-state cumulative displacements than glass-fiber-reinforced composite friction materials (Gatke 81, 82, 397, and 398), which indicated a faster establishment of the break-in effect. This is because for the composite-metallic friction interfaces tested in this study, the break-in effect is mainly attributed to the worn-out of surface asperities, which induces an increase in the real contact area and the adhesive friction [29,57–59]. Cotton fibers had a lower hardness than glass fibers, which potentially made the worn-out of surface asperities easier than that of glass fibers. Except for Gatke 82, a higher normal load overall resulted in a faster break-in process. This is because a higher normal load potentially enhanced the process of wearing out surface asperities.

Fig. 21 also presents the normalized bolt load ($\frac{N}{N_{target}}$) history within the break-in tests. It can be observed that bolt load loss was most significant within break-in tests one (Brk1) and was reduced as break-in tests continued. The bolt load variation reflected the wear mechanism of the friction interface. At the beginning of sliding, besides the break-in process, the wear-in process also happened, in which a steady-state wear rate was to be reached [29]. According to the non-linear model of the wear behavior [60], the wear rate was higher at the beginning of sliding. A higher wear rate increased the wear volume, causing the friction shims to be thinner. This mechanism induced a higher bolt load loss as observed in break-in tests one. As the cumulative displacement increased, the wear rate was reduced, making the increase of the wear volume slower and therefore, induced a smaller bolt load loss as observed in break-in tests two and three.

4.4.4. *Effect of sliding velocity*

Fig. 22 shows the assessment of the effect of sliding velocities on the response of the friction interface. In Fig. 22, each black circular marker represents the mean $\mu_{computed}$ of one sliding travel, and the computation method of $\mu_{computed}$ was the same as in Section 4.4.3. The x-axis, starting from zero, represents the testing period of Test IDs 5~10 with the ten seconds dwell time between tests being excluded. Fig. 22 shows the evolution of $\mu_{computed}$ in Test IDs 5~10. In Fig. 22, light red lines represent the time history of the absolute sliding velocity, which was computed from the recorded displacement response. It is noted that for test groups with high normal load, the peak sliding velocity of Test IDs 7 and 8 was lower than the target imposed peak sliding velocity in Fig.

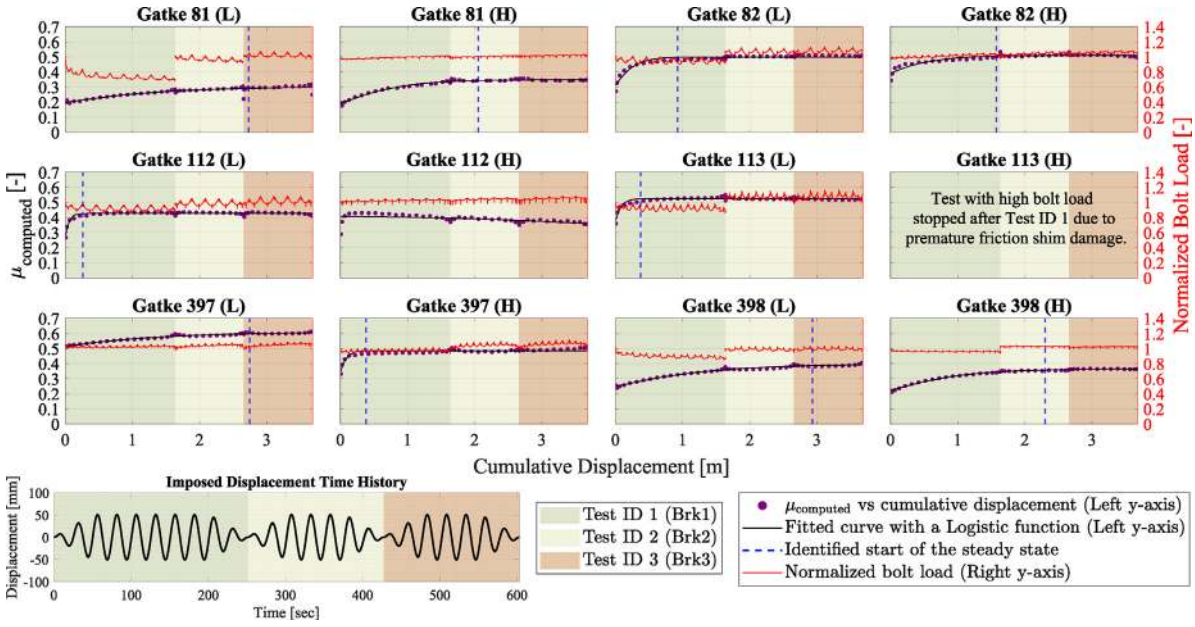


Fig. 21. Assessment of the break-in effect.

Table 5
Summary of break-in effect assessment results.

Test group	Initial COF from test ID 1 μ_{ini}	Logistic function regression analysis			Mean COF from test ID 4 $\overline{\mu_4}$	Relative difference computation	
		R^2	Identified steady-state COF μ_{ss}	Identified steady-state cumulative displacement [m]		$\delta_{ss-4}=\frac{\overline{\mu_4}-\mu_{ss}}{\mu_{ss}}$	$\delta_{ini-ss}=\frac{\mu_{ss}-\mu_{ini}}{\mu_{ini}}$
Gatke 81 (L)	0.213	0.83	0.303	2.730	0.326	7.51%	42.27%
Gatke 81 (H)	0.194	0.98	0.348	2.051	0.355	1.92%	79.15%
Gatke 82 (L)	0.272	0.92	0.499	0.924	0.518	3.73%	83.30%
Gatke 82 (H)	0.343	0.88	0.510	1.574	0.490	−3.85%	48.67%
Gatke 112 (L)	0.268	0.90	0.427	0.259	0.421	−1.52%	59.65%
Gatke 112 (H)	0.289	0.32	N/A	N/A	0.356	N/A	N/A
Gatke 113 (L)	0.378	0.88	0.525	0.375	0.527	0.40%	38.88%
Gatke 113 (H)	N/A						
Gatke 397 (L)	0.518	0.96	0.613	2.742	0.608	−0.80%	18.35%
Gatke 397 (H)	0.332	0.82	0.486	0.382	0.509	4.85%	46.27%
Gatke 398 (L)	0.265	0.97	0.397	2.930	0.422	6.48%	49.78%
Gatke 398 (H)	0.221	0.99	0.365	2.300	0.380	4.19%	65.29%

11. This was attributed to the stalling of the testing machine caused by the hydraulic supply capacity limitation.

The mean coefficient of friction for Test ID i, termed $\overline{\mu_i}$, is summarized in Table 6 for Test IDs 5~10 for all test groups except for Test Group Gatke 113 (H). The relative difference between mean coefficients of friction for Test ID i ($\overline{\mu_i}$) within Test IDs 5~10 and the mean coefficient of friction for Test ID 5 ($\overline{\mu_5}$) is computed as $\delta_{i\text{-}5}=\frac{\overline{\mu_i}-\overline{\mu_5}}{\overline{\mu_5}}$. The computed relative difference for all test groups except for Test Group Gatke 113 (H) is also reported in Table 6 and is shown in Fig. 23. From Fig. 22 and Table 6, it is observed that except for Test Groups Gatke 398 (L) and (H), an increase in the sliding velocity overall induced a decrease in the coefficient of friction μ. Fig. 23 shows that the decrease in μ was more significant in test groups with high normal load than test groups with low normal load. Fig. 23 also shows that for test groups with glass-fiber-reinforced composite friction materials such as Test Groups Gatke 81 (H), Gatke 82 (H), and Gatke 397 (H), μ exhibited an increase in follow-up tests with lower sliding velocities; while for test groups with cotton-fiber-reinforced composite friction materials such as Test Groups Gatke 112 (L) and (H), a further decrease in μ was observed in follow-up tests with lower sliding velocities.

Similar velocity-dependent variation of the coefficient of friction has been observed in past experimental tests of composite-metallic friction interfaces [1,61]. Bowden and Tabor's adhesive friction theory [25, 62] is introduced herein to explain the observed velocity-dependent variation of the coefficient of friction. Fig. 24 presents a schematic explanation of Bowden and Tabor's adhesive friction theory. The theory suggests that when two surfaces are in contact under a certain normal pressure, the contact happens at the highest peaks, and the real contact area is much smaller than the total contact area. Locally, the normal stress could be high enough so that plastic deformation of the materials occurs. Adhesion junctions are formed at the contact points. When sliding occurs between these two surfaces, the friction force generated at the friction interface comes from two sources: shearing of the adhesion junctions, and the plowing of hard materials into soft materials. For composite-metallic friction interfaces used in structural engineering applications, the contribution of plowing could be considered negligible. Fig. 25(a) presents the state of the friction interface after the establishment of the break-in effect (i.e., the friction interface reached a steady state as defined in Section 4.4.3) as at the beginning of Test ID 5, represented schematically by a single adhesion junction. In this state, the normal force is termed N; the friction force is termed f_{ss}; the real contact area is termed $A_{j,ss}$; the normal pressure developed at this adhesion junction is termed σ_{ss}; the shear strength of this adhesion junction is termed τ_{ss}; the coefficient of friction of the friction interface, which is the steady state coefficient of friction, is termed μ_{ss}. By force

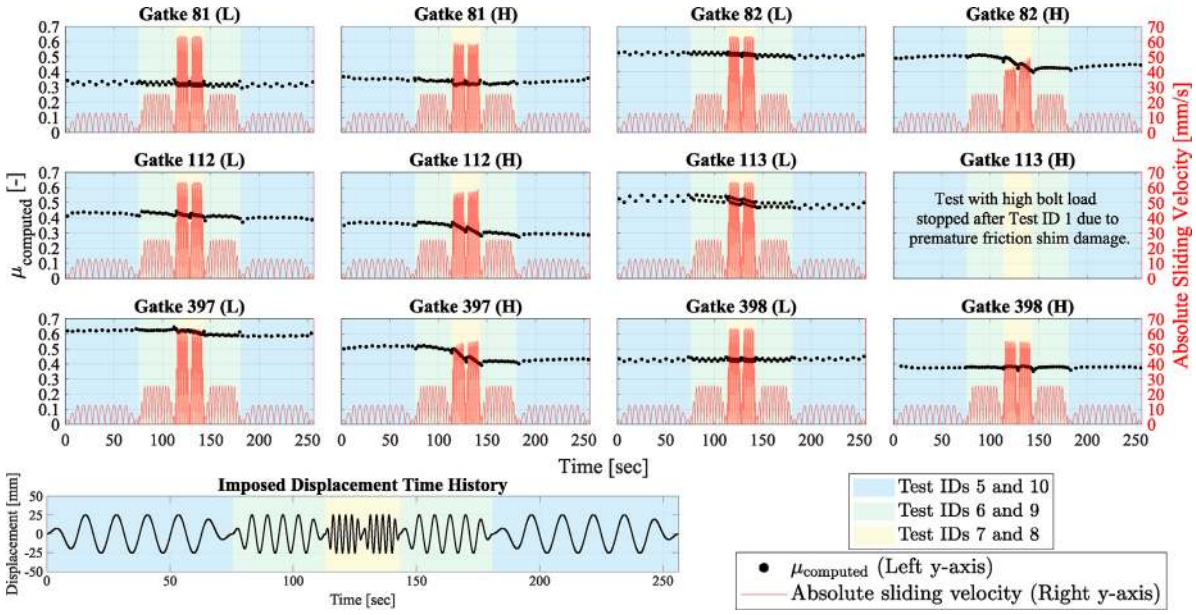


Fig. 22. Assessment of effect of sliding velocity (Test IDs 5~10).

Table 6
Summary of mean COF ($\overline{\mu_i}$) and relative difference between $\overline{\mu_i}$ and $\overline{\mu_5}$ (δ_{i-5}) for Test IDs 5~10.

Test Group	$\overline{\mu_5}$ ($\delta_{5\text{-}5}$)	$\overline{\mu_6}$ ($\delta_{6\text{-}5}$)	$\overline{\mu_7}$ ($\delta_{7\text{-}5}$)	$\overline{\mu_8}$ ($\delta_{8\text{-}5}$)	$\overline{\mu_9}$ ($\delta_{9\text{-}5}$)	$\overline{\mu_{10}}$ ($\delta_{10\text{-}5}$)
Gatke 81 (L)	0.33 (0.00%)	0.32 (−3.03%)	0.32 (−3.03%)	0.32 (−3.03%)	0.31 (−6.06%)	0.32 (−3.03%)
Gatke 81 (H)	0.35 (0.00%)	0.35 (0.00%)	0.32 (−8.57%)	0.32 (−8.57%)	0.33 (−5.71%)	0.34 (−2.86%)
Gatke 82 (L)	0.52 (0.00%)	0.52 (0.00%)	0.52 (0.00%)	0.51 (−1.92%)	0.51 (−1.92%)	0.50 (−3.85%)
Gatke 82 (H)	0.50 (0.00%)	0.51 (2.00%)	0.48 (−4.00%)	0.44 (−12.00%)	0.42 (−16.00%)	0.44 (−12.00%)
Gatke 112 (L)	0.43 (0.00%)	0.43 (0.00%)	0.42 (−2.33%)	0.42 (−2.33%)	0.41 (−4.65%)	0.40 (−6.98%)
Gatke 112 (H)	0.37 (0.00%)	0.36 (−2.70%)	0.34 (−8.11%)	0.31 (−16.22%)	0.30 (−18.92%)	0.29 (−21.62%)
Gatke 113 (L)	0.53 (0.00%)	0.53 (0.00%)	0.51 (−3.77%)	0.50 (−5.66%)	0.48 (−9.43%)	0.48 (−9.43%)
Gatke 113 (H)	N/A					
Gatke 397 (L)	0.62 (0.00%)	0.63 (1.61%)	0.62 (0.00%)	0.61 (−1.61%)	0.59 (−4.84%)	0.59 (−4.84%)
Gatke 397 (H)	0.52 (0.00%)	0.51 (−1.92%)	0.47 (−9.62%)	0.43 (−17.31%)	0.42 (−19.23%)	0.43 (−17.31%)
Gatke 398 (L)	0.43 (0.00%)	0.43 (0.00%)	0.43 (0.00%)	0.43 (0.00%)	0.43 (0.00%)	0.43 (0.00%)
Gatke 398 (H)	0.38 (0.00%)	0.38 (0.00%)	0.38 (0.00%)	0.38 (0.00%)	0.38 (0.00%)	0.38 (0.00%)

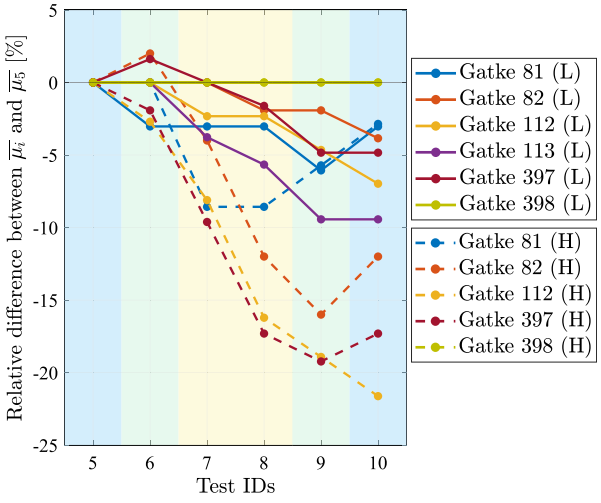


Fig. 23. Relative difference between $\overline{\mu_i}$ and $\overline{\mu_5}$ in Test IDs 5~10.

equilibrium, the friction interface has:

$$N = A_{j,ss}\sigma_{ss}$$
$$f_{ss} = A_{j,ss}\tau_{ss}$$
$$\mu_{ss} = \frac{f_{ss}}{N} = \frac{A_{j,ss}\tau_{ss}}{A_{j,ss}\sigma_{ss}} = \frac{\tau_{ss}}{\sigma_{ss}} \tag{4}$$

Fig. 25(b) presents the state of the friction interface under an increased sliding velocity during Test IDs 7~8. In the discussion of the effect of the sliding velocity on the response of the friction interface, the normal load N is assumed to remain relatively constant. A detailed discussion on the variation of the normal load is presented in Section 4.4.8. Under a higher sliding velocity, the wear rate increased. The increased wear rate resulted in increased generation and accumulation of wear particles at the friction interface. The accumulation of wear particles potentially reduced the shear strength of the adhesion junction from τ_{ss} to τ_f ($\tau_f < \tau_{ss}$). In addition, the increased wear rate potentially caused the real contact area to reduce from $A_{j,ss}$ to $A_{j,f}$ [1], resulting in an increased normal pressure at the adhesion junction ($\sigma_f > \sigma_{ss}$). For this new state, the friction interface has:

$$\mu_f = \frac{\tau_f}{\sigma_f} < \frac{\tau_{ss}}{\sigma_{ss}} = \mu_{ss} \tag{5}$$

Eq. (5) explained the observed decrease in the coefficient of friction μ associated with the increase in the sliding velocity in Test IDs 7~8 as shown in Figs. 22 and 23.

Fig. 25(c) presents the state of the friction interface under a lower sliding velocity during Test IDs 9~10. Under a lower sliding velocity, the wear rate decreased and in the meantime, previously generated wear particles got evacuated from the friction interface. The evacuation of wear particles potentially induced an increase in the shear strength of the adhesion junction from τ_f to τ_s ($\tau_s > \tau_f$). In addition, under a lower sliding velocity, the rejuvenation of the friction interface potentially caused the real contact area to increase from $A_{j,f}$ to $A_{j,s}$ [1], resulting

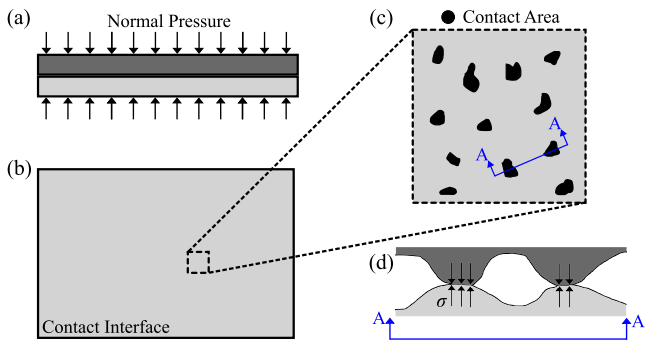


Fig. 24. Schematic explanation of Bowden and Tabor's adhesive friction theory: (a) Two plates are clamped together under a certain normal pressure (b) Top view of the contact interface (c) Zoomed-in top view of the contact interface, with real contact areas being exaggerated (d) Zoomed-in elevation view of the contact interface at Section A-A; a normal pressure of σ is developed at the adhesion junction.

in a decrease in the normal pressure at the adhesion junction ($\sigma_s < \sigma_f$). For this new state, the friction interface has:

$$\mu_s = \frac{\tau_s}{\sigma_s} > \frac{\tau_f}{\sigma_f} = \mu_f \tag{6}$$

Eq. (6) explained the observed increase in the coefficient of friction μ associated with a lower sliding velocity in Test IDs 9~10 as shown in Figs. 22 and 23.

In summary, the above explanation highlights the competing effect of two processes: wear particles generation and accumulation at the friction interface versus wear particles evacuation from the friction interface. When the sliding velocity was relatively high, the rate of wear particles generation and accumulation at the friction interface was effectively higher than the rate of wear particles evacuation from the friction interface, and this tended to induce a decrease in the coefficient of friction (as during Test IDs 7~8). In contrast, when the sliding velocity was relatively low, the rate of wear particles generation and accumulation at the friction interface was effectively lower than the rate of wear particles evacuation from the friction interface, and this tended to induce an increase in the coefficient of friction (as during Test IDs 9~10).

Based on the explanation above, the effect of material constituents on the velocity-dependent frictional behavior is discussed herein. In Test IDs 9~10, the difference between the frictional behavior of friction interfaces with glass-fiber-reinforced composite friction materials and those with cotton-fiber-reinforced composite friction materials can be potentially explained as follows: Glass fibers have higher hardness than cotton fibers, and therefore, glass fibers potentially enhanced the evacuation of wear particles from the friction interface. For friction interfaces with glass-fiber-reinforced composite friction materials, a larger percentage of increase in the coefficient of friction was thus observed in Test IDs 9~10. For friction interfaces with cotton-fiber-reinforced composite friction materials, the effect of the evacuation of wear particles was less significant; consequently, a similar or further decrease in the coefficient of friction was observed in Test IDs 9~10.

In addition to the observations above, comparing the results of Test Groups Gatke 81 (H) and Gatke 82 (H), it is found that Gatke 81 (H) exhibited a less reduction in the coefficient of friction in Test IDs 7~8 and a larger percentage of increase in the coefficient of friction in Test IDs 9~10. Hypothetically this was attributed to the contribution of acrylic fibers and aramid fibers in Gatke 81. Comparing the results of Test Groups Gatke 81 (H), Gatke 82 (H) and Gatke 397 (H), it is found that Gatke 81 (H) and Gatke 82 (H) exhibited a larger percentage of increase in the coefficient of friction in Test IDs 9~10 than Gatke 397 (H). Hypothetically the presence of abrasive particles (yellow iron oxide, green chromium (III) oxide, and aluminum oxide) in Gatke 81 and 82 enhanced the evacuation of wear particles. It is noteworthy that

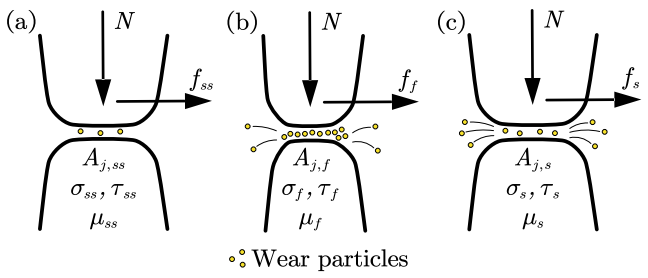


Fig. 25. Schematic representation of the state of the friction interface (a) at the beginning of Test ID 5 (b) during Test IDs 7~8 and (c) during Test IDs 9~10.

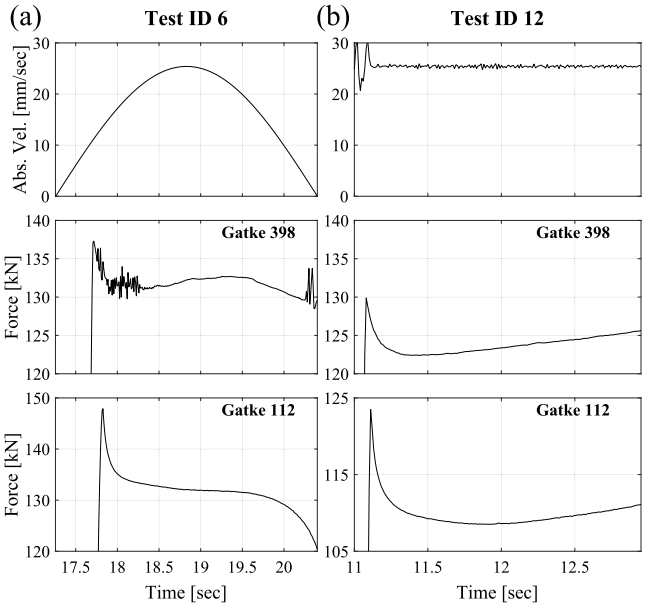


Fig. 26. (a) Absolute sliding velocity history and recorded friction force history of one selected representative sliding travel from Test ID 6 in Test Groups Gatke 398 (H) and Gatke 112 (H) (b) Absolute sliding velocity history and recorded friction force history of one selected representative sliding travel from Test ID 12 in Test Groups Gatke 398 (H) and Gatke 112 (H).

Gatke 398 exhibited the least significant velocity-dependent frictional behavior among the composite friction materials tested in this study. In both Gatke 398 (L) and (H), the average coefficient of friction $\overline{\mu}$ was the same for all tests within Test IDs 5~10. Hypothetically this was attributed to the contribution of graphite, Teflon, and molybdenum disulfide (MoS_2), which assisted in controlling the wear rate of the friction interface under different sliding velocities.

4.4.5. *Oscillation in the friction force response*

Fig. 26(a) and (b) present the absolute sliding velocity history and the corresponding recorded friction force history of one selected representative sliding travel from Test IDs 6 and 12 in Test Groups Gatke 398 (H) and Gatke 112 (H). From Fig. 26(a) and (b), it can be observed that oscillation occurred in the friction force response of Gatke 398 and was associated with lower sliding velocities. Although not shown, the same observation applied to Gatke 81, 82, and 397. It is also observed that oscillation did not occur in the friction force response of Gatke 112, regardless of the sliding velocity. Although not shown, the same observation applied to Gatke 113.

Oscillation in the friction force response associated with lower sliding velocities was attributed to the stick–slip behavior of the friction interface. The stick–slip behavior of composite-metallic friction interfaces has been studied and was attributed to the change of the

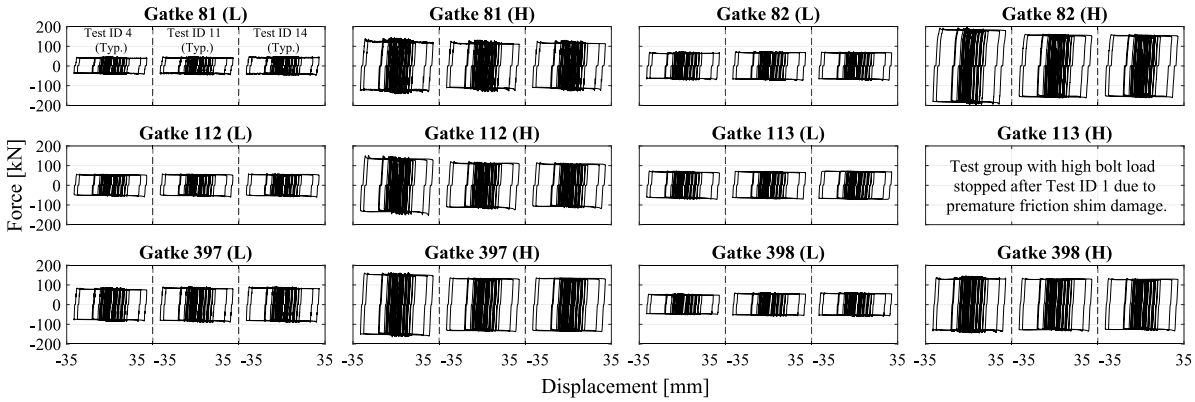


Fig. 27. Force–displacement responses of the tested friction interfaces under earthquake-type input excitation (Test IDs 4, 11, and 14).

surface topography of the friction interface [61,63,64]. For friction interfaces with glass-fiber-reinforced composite friction materials, the accumulation of wear particles tended to be more localized as hard glass fibers at the friction interface facilitated the accumulation of wear particles around them. The localized accumulation and evacuation of wear particles enhanced the stick–slip behavior of the friction interface, inducing oscillation in the friction force response under low sliding velocities [61,64]. In contrast, for friction interfaces with cotton-fiber-reinforced composite friction materials, the accumulation and evacuation of wear particles tended to be more uniform across the friction interface, as softer cotton fibers provided limited supports for localized accumulation of wear particles. Therefore, the stick–slip behavior of friction interfaces with cotton-fiber-reinforced composite friction materials was insignificant. It should be noted that for earthquake structural engineering applications, the frequency of the oscillation in the friction force response is high relative to the frequencies of interest at the structural and nonstructural component level and the magnitude of the oscillation is low relative to typical force demands of friction-based structural components. The effect of the stick–slip behavior of composite-metallic friction interfaces could be considered insignificant for earthquake structural engineering applications.

4.4.6. Response of friction interfaces under earthquake-type input excitation

Fig. 27 shows the recorded force versus displacement responses of the tested friction interfaces under earthquake-type input excitation. For all the tested friction interfaces, the shape of the force–displacement response was close to a rectangle and thus could be idealized as a Coulomb-type force–displacement response. The force–displacement response shows the pinching displacement at zero force due to the gap between the steel channel and the friction shim. The pinching displacement at zero force was considered small and could be further reduced by a tighter tolerance control in machining the steel channels.

Fig. 28 shows the evolution of the coefficient of friction of the tested friction interfaces with respect to the increase of the cumulative displacement under earthquake-type input excitation. In Fig. 28, each circular marker represents the mean $\mu_{computed}$ of one sliding travel and its corresponding mean cumulative displacement within this sliding travel. The computation method was the same as in Section 4.4.3. The mean coefficients of friction within each Test ID ($\overline{\mu}$) are reported in the figure. It can be observed that within each Test ID, the coefficient of friction maintained at a relatively constant level, which was consistent with the rectangular force–displacement responses as shown in Fig. 27. For some test groups, a difference in $\overline{\mu}$ between Test IDs can be observed, and the difference is attributed to the effect of the sliding history. As described in Section 3.3.4, between Test IDs 4 and 11, Test IDs 5~10 assessed the effect of sliding velocities on the response of the friction interface. In some test groups, the effect of sliding velocity from Test IDs 5~10 got carried over to follow-up tests, i.e., Test IDs 11 and 14. The details of velocity-dependent frictional behavior have been discussed in Section 4.4.4.

From Fig. 28, the effect of the normal load level on the magnitude of the coefficient of friction can also be observed. Gatke 81 (H) exhibited a higher coefficient of friction than Gatke 81 (L). Hypothetically this was attributed to the contribution of aramid fibers. In contrast, for Gatke 82, 112, 397, and 398, a decrease in the coefficient of friction was observed when the normal load was increased from low to high.

4.4.7. Effect of dwell time

Fig. 29 shows the data used to assess the effect of the dwell time on the frictional behavior. The relative difference between the mean coefficient of friction of the prior test (termed $\overline{\mu}_{pr}$) and the mean coefficient of friction of its corresponding posterior test (termed $\overline{\mu}_{po}$) was computed as $\frac{\overline{\mu}_{po}-\overline{\mu}_{pr}}{\overline{\mu}_{pr}}$ and was plotted against its corresponding dwell time (DT10s, DT10m, and DT30m). As shown in the imposed displacement time history plot (truncated to the first 100 seconds for presentation purposes) of one prior test and its corresponding posterior test, to exclude the effect of the cumulative displacement on the coefficient of friction, for prior tests, the last four sliding travels were selected for the computation of $\overline{\mu_{pr}}$, and for posterior tests, the first four sliding travels were selected for the computation of $\overline{\mu_{po}}$.

Fig. 29 shows that the dwell time overall increased the coefficient of friction in cases of Gatke 81, 82, 112, and 398. Comparing the result of DT30m with DT10s and DT10m, it is observed that a longer dwell time overall induced a larger increase in the coefficient of friction. The increase in the coefficient of friction was less than 10% except for Gatke 112 (H). The increase in the coefficient of friction associated with the dwell time can be attributed to the increase in the real contact area between two contact surfaces of the friction interface [1,25,65]. Fig. 29 also shows that for Gatke 113 and 397, the dwell time induced a decrease in the coefficient of friction in all cases. The effect of dwell time on the response of friction interfaces formed by Gatke 113 and Gatke 397 in contact with low-carbon structural steel requires further investigation.

4.4.8. Bolt load variation

Fig. 30(a) shows the time history of the normalized bolt load (N/N_{target}) in all test groups. In Fig. 30(a), the bolt load time histories during the bolt retightening process and the dwell time were excluded. The normalized bolt load variation was similar in all tests. The instantaneous sliding velocity appeared to affect the bolt load. An increase in instantaneous sliding velocities resulted in a relatively small increase in the bolt load, such as in Test IDs 7 and 8. A lower instantaneous sliding velocity overall resulted in a decrease in the bolt load, such as in Test IDs 9 and 10. Fig. 30(b) shows the time history of the normalized bolt load of Test IDs 7 and 8 in Test Group Gatke 398 (H) as an example to further discuss this effect. In Fig. 30(b), the time history of the

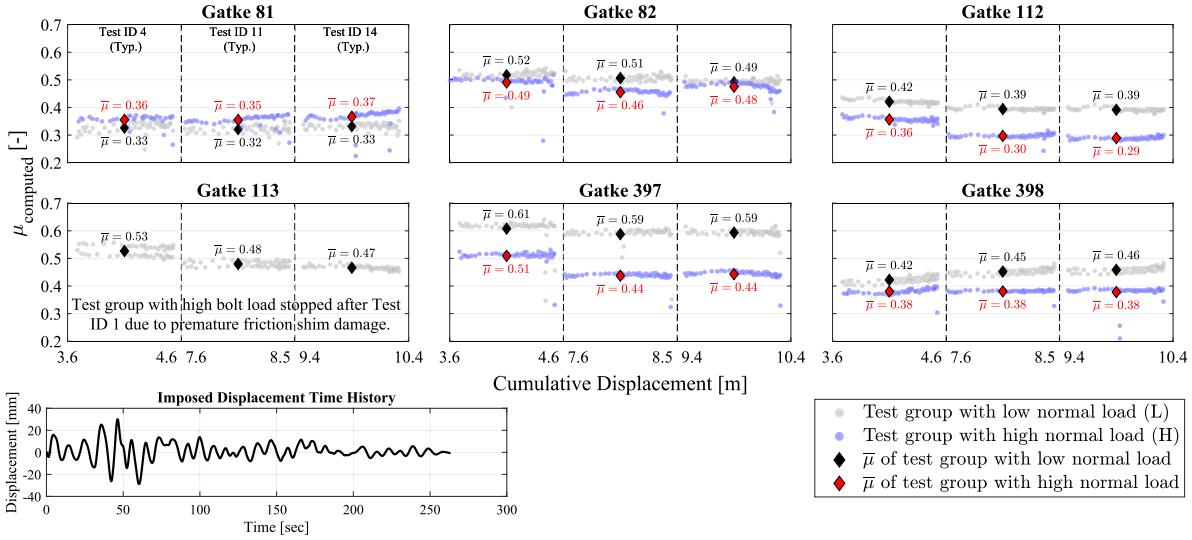


Fig. 28. Evolution of μ of the friction interfaces under earthquake-type input excitation (Test IDs 4, 11, and 14).

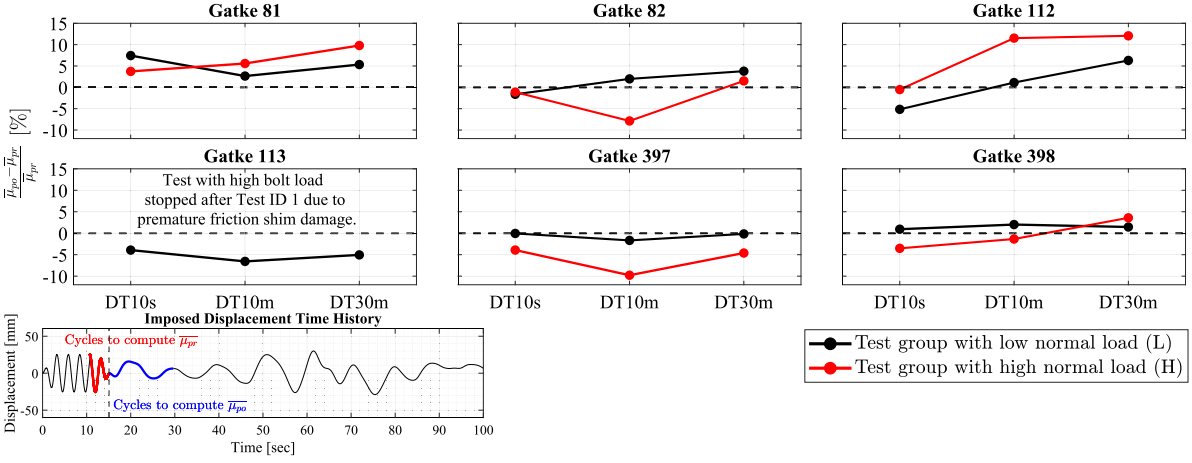


Fig. 29. Assessment of the effect of dwell time (Test IDs 15~20).

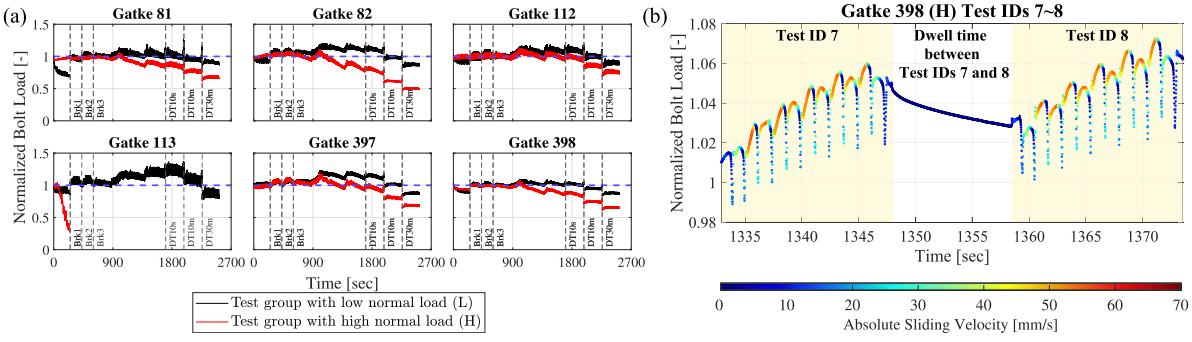


Fig. 30. (a) Normalized bolt load time history of all test groups and (b) Normalized bolt load time history of Test IDs 7 and 8 in Test Group Gatke 398 (H); the color of the marker is defined based on the instantaneous absolute sliding velocity.

normalized bolt load during the dwell time between Test ID 7 and Test ID 8 is also presented. The colorbar defines the magnitude of the instantaneous sliding velocity. As the instantaneous velocity increased, the instantaneous bolt load increased. As the instantaneous velocity decreased, the instantaneous bolt load decreased. An overall increase of the bolt load was observed during the duration of Test ID 7 and during the duration of Test ID 8. A reduction in the bolt load was observed during the dwell time between Test ID 7 and Test ID 8.

Section 4.4.4 explains the effect of sliding velocities on the accumulation and evacuation of wear particles. The same mechanics can be adopted here to explain the variation of bolt load with respect to the variation of the instantaneous sliding velocity, as follows: When the instantaneous sliding velocity increased, the wear rate increased. As a result, the rate of accumulation of wear particles at the friction interface increased. As the cumulative sliding under relatively high

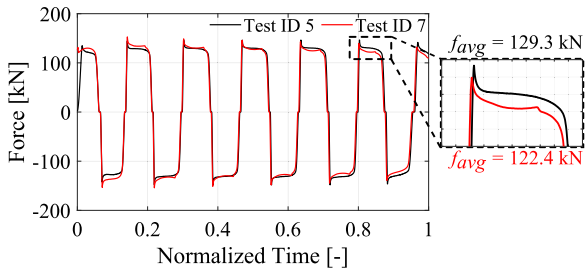


Fig. 31. Recorded force response time history of Test IDs 5 and 7 from Test Group Gatke 112 (H).

instantaneous sliding velocities increased, the unstructured accumulation of wear particles effectively increased the total thickness of the bolted assembly, which in turn led to bolt elongation and an increase in the bolt load. Under a relatively low instantaneous sliding velocity, the effect of the evacuation of wear particles became more significant than the effect of the accumulation of wear particles. As the cumulative sliding under relatively low instantaneous sliding velocities increased, the evacuation of wear particles reduced the total thickness of the bolted assembly, which in turn led to bolt shortening and a decrease in the bolt load. As shown in Fig. 30(b), during Test IDs 7 and 8, the effect of the unstructured accumulation of wear particles in the friction interface during relatively high-velocity sliding motions outweighs the effect of the evacuation of wear particles during relative low-velocity sliding motions. Therefore, the increase in the bolt load was cumulative and an overall increased bolt load during the durations of Test IDs 7 and 8 was observed. The increase in the bolt load during the durations of Test IDs 7 and 8 could be considered small (approximately 5%) in the context of earthquake structural engineering applications. The bolt load loss during dwell time was attributed to the compaction of unstructured accumulated wear particles.

As demonstrated in Section 4.4.4, relatively high-velocity sliding motions overall induced a decrease in the coefficient of friction μ. As explained in this section, relatively high-velocity sliding motions overall resulted in an increase in the bolt load N. According to Coulomb's friction equation $f = \mu N$, it can be observed that the effect of sliding velocities on μ and N cancels out each other on the product f. Therefore, for a friction-based structural component, the friction force generated is possible to maintain relatively constant under high sliding velocities. Fig. 31 presents the recorded force response time history of the friction interface in Test Group Gatke 112 (H) and in Test IDs 5 and 7 as an example, plotted in the normalized time scale for comparison purposes. From Table 6, it is learned that the coefficient of friction of this friction interface was reduced by 8.11% in Test ID 7 compared with Test ID 5. In the sliding travel highlighted in Fig. 31, the average sliding force (termed f_{avg}) of this sliding travel in Test ID 5 was 129.3 kN and the same quantity in Test ID 7 was 122.4 kN. The reduction in the sliding force was 5.3%, lower than 8.11%, because of the effect of the increase in the bolt load as explained above. Practically, the sliding force generated by the friction interface in this case can be considered relatively constant in Test IDs 5 and 7.

In addition to the observations above, it is also observed that the normal load level had an impact on the bolt load loss. Test groups under high normal load exhibited more normalized bolt load loss toward the end of the loading protocol than test groups under low normal load. This is because the higher normal load induced more wear of the composite material friction shims and consequently resulted in a more significant reduction in the total thickness of the bolted assembly, which in turn led to a more significant decrease in the bolt load toward the end of the loading protocol.

5. Conclusions

This paper presented an experimental study focused on characterizing the mechanical properties of composite friction materials and the tribological properties of composite to low-carbon structural steel friction interfaces for use in friction-based structural components for earthquake structural engineering applications. A systematic testing program was proposed. The testing program included the coupon tensile test, the plate bearing test, the bolt relaxation test, and the friction test. The friction test considered the normal load level, loading frequencies, sliding velocities, velocity profiles (earthquake vs. sinusoidal vs. linear), and sliding histories (the cumulative displacement, the dwell time, and previous sliding events) as the testing parameters. The effect of these parameters on the friction sliding force, the bolt load, and the experimentally derived coefficient of friction was presented. Six types of phenolic-resin-based fiber-reinforced composite friction materials were tested using the proposed testing program. Based on the experimental testing results, the following conclusions were made:

- The flash compression molding process may result in manufacturing of materials with regions of lower concentration of phenolic resin than anticipated. This potential manufacturing imperfection was shown to exacerbate delamination of the composite material, characterized by bond failure observed during the coupon tensile test.
- The percentage of bolt load loss due to the creep effects in the composite friction materials ranged from 4.5% to 15%. Possible flash compression molding manufacturing defects can lead to a lower concentration of phenolic resin, resulting in lower bonding and adhesion between the matrix and fibers. This mechanism can induce exacerbated through-thickness creep effects, and consequently an increased percentage of bolt load loss. The bolt relaxation test results highlighted the importance of quality control in the manufacturing of composite friction materials for friction-based structural components.
- The break-in effect depends on the material constituents of the composite friction materials and the normal load level. Cotton-fiber-reinforced composite friction materials compared with glass-fiber-reinforced composite friction materials required less cumulative sliding to establish a steady-state coefficient of friction. A higher normal load increased the wear rate for both cotton- and glass-fiber-reinforced composite friction materials. As a result, a steady-state coefficient of friction was reached with less cumulative sliding.
- Friction tests with different sliding velocities showed a general trend where an increase in the sliding velocity led to a reduction in the coefficient of friction while lower sliding velocities overall resulted in an increase in the coefficient of friction. The reduction in the coefficient of friction was attributed to higher wear rates under higher sliding velocities and accumulation of wear particles, which decreased the shear strength of the adhesion junction and potentially the real contact area. The increase in the coefficient of friction was attributed to the evacuation of wear particles, which increased the shear strength of the adhesion junction, and potentially an increase in the real contact area. A higher normal load was shown to enhance the velocity-dependent frictional behavior.
- Constituents of composite materials appeared to affect velocity-dependent behavior of composite-metallic friction interfaces. The presence of glass fibers and abrasive particles such as yellow iron oxide, green chromium (III) oxide, and aluminum oxide in the material constituent appeared to enhance the evacuation of wear particles. Among the friction interfaces tested in this study, the friction interface with the composite friction material Gatke 398 (consisting of phenolic resin, glass fibers, graphite, Teflon and molybdenum disulfide MoS_2) in contact with low-carbon

structural steel exhibited the most stable frictional behavior under different sliding velocities. Hypothetically this was attributed to the contribution of graphite, Teflon, and molybdenum disulfide MoS_2.

- Friction interfaces with glass-fiber-reinforced composite friction materials exhibited oscillations in the force response at low sliding velocities due to the stick–slip behavior of the friction interface. The stick–slip behavior was attributed to the localized accumulation and evacuation of wear particles, which was enhanced by hard glass fibers. In contrast, friction interfaces with cotton-fiber-reinforced composite friction materials did not exhibit oscillations in the force response. The effect of the stick–slip behavior of composite-metallic friction interfaces could be considered insignificant for earthquake structural engineering applications.
- The increased dwell time increased the coefficient of friction with exception the test cases that used Gatke 113 and Gatke 397 which require further investigation.
- The friction-based structural component with composite-metallic friction interfaces tested in this study exhibited velocity-dependent bolt load variation because of the wear mechanism of the friction interface. Higher sliding velocities tended to induce an increase in the bolt load due to increased wear debris generation and accumulation while lower sliding velocities tended to induce a reduction in the bolt load due to wear debris evacuation. In addition, a higher normal load overall induced more wear of the composite friction material and therefore, induced more bolt load loss toward the end of the test.
- Considering the results of the mechanical and tribological characterization of materials presented in this study, composite materials that consist of phenolic resin, glass fibers, graphite, Teflon and molybdenum disulfide MoS_2 are among the most suitable materials for use in friction-based structural components for earthquake structural engineering applications. More in-depth studies can be conducted using techniques such as Scanning Electron Microscopy (SEM) and Energy-dispersive X-ray (EDX) to gain a better understanding of the micro-level friction mechanism of this type of material; this will support the future development of high-performance composite friction materials for earthquake structural engineering applications.

CRediT authorship contribution statement

Kaixin Chen: Writing – original draft, Visualization, Validation, Software, Methodology, Investigation, Formal analysis, Data curation, Conceptualization. **Georgios Tsampras:** Writing – review & editing, Supervision, Resources, Project administration, Methodology, Investigation, Funding acquisition, Data curation, Conceptualization. **Shivaglal Cheruvalath:** Writing – review & editing, Resources, Investigation. **Mary Thundathil:** Writing – review & editing, Resources, Investigation.

Declaration of Generative AI and AI-assisted technologies in the writing process

During the preparation of this work, the authors used ChatGPT in order to improve the readability and language of the manuscript. After using this tool, the authors reviewed and edited the content as needed and take full responsibility for the content of the published article.

Declaration of competing interest

The authors declare the following financial interests/personal relationships which may be considered as potential competing interests: Kaixin Chen reports financial support was provided by Precast Prestressed Concrete Institute. Kaixin Chen reports equipment, drugs, or supplies was provided by Scan-Pac Mfg., Inc. If there are other authors, they declare that they have no known competing financial interests or personal relationships that could have appeared to influence the work reported in this paper.

Acknowledgments

The authors are grateful for financial support provided by Structural Engineering Distinguished Fellowship and additional support from the Department of Structural Engineering at UC San Diego, and financial support provided by Daniel P. Jenny Fellowship from Precast/Prestressed Concrete Institute (PCI). Composite friction materials donated by ScanPac Mfg., Inc. are kindly appreciated. Moreover, this work was performed in part at the San Diego Nanotechnology Infrastructure (SDNI) of UCSD, a member of the National Nanotechnology Coordinated Infrastructure, which is supported by the National Science Foundation (Grant ECCS-2025752). Any opinions, findings, and conclusions expressed in this paper are those of the authors and do not necessarily reflect the views of the parties acknowledged here.

Data availability

Data will be made available on request.

References

[1] Tsampras G, Sause R, Fleischman RB, Restrepo JI. Experimental study of deformable connection consisting of friction device and rubber bearings to connect floor system to lateral force resisting system. Earthq Eng Struct Dyn 2018;47(4):1032–53. http://dx.doi.org/10.1002/eqe.3004.
[2] Soong TT, Dargush GF. Passive energy dissipation systems in structural engineering. Wiley; 1997.
[3] Chen K, Tsampras G, Lee K. Structural connection with predetermined discrete variable friction forces. Resil Cities Struct 2023;2(1):1–17. http://dx.doi.org/10.1016/j.rcns.2023.02.006.
[4] Jaisee S, Yue F, Ooi YH. A state-of-the-art review on passive friction dampers and their applications. Eng Struct 2021;235:112022. http://dx.doi.org/10.1016/j.engstruct.2021.112022.
[5] Mokha A, Constantinou M, Reinhorn A. Teflon bearings in base isolation I: Testing. J Struct Eng 1990;116(2):438–54. http://dx.doi.org/10.1061/(ASCE)0733-9445(1990)116:2(438).
[6] Fitzgerald TF, Anagnos T, Goodson M, Zsutty T. Slotted bolted connections in aseismic design for concentrically braced connections. Earthq Spectra 1989;5(2):383–91. http://dx.doi.org/10.1193/1.1585528.
[7] Tremblay R. Seismic behavior and design of friction concentrically braced frames for steel buildings (Ph.D. thesis), The University of British Columbia; 1993.
[8] Grigorian CE, Yang TS, Popov EP. Slotted bolted connection energy dissipators. Earthq Spectra 1993;9(3):491–504. http://dx.doi.org/10.1193/1.1585726.
[9] Petty GD. Evaluation of a friction component for a post-tensioned steel connection (Master thesis), Lehigh University; 1999.
[10] Chi B, Uang CM. Dynamic testing of full-scale slotted bolted connections. TR-99/05, University of California, San Diego; 2000.
[11] Golondrino JC, MacRae GA, Chase JG, Rodgers GW, Clifton GC. Behaviour of asymmetrical friction connections using different shim materials. In: Proceedings of the 2012 NZSEE Annual Technical Conference. New Zealand Society for Earthquake Engineering; 2012.
[12] Latour M, Piluso V, Rizzano G. Experimental analysis on friction materials for supplemental damping devices. Constr Build Mater 2014;65:159–76. http://dx.doi.org/10.1016/j.conbuildmat.2014.04.092.
[13] Qin Y, Zhao K-X, Shu G-P, Ke L. Experimental study on frictional behavior of different structural materials. Structures 2023;49:557–69. http://dx.doi.org/10.1016/j.istruc.2023.01.142.
[14] Liu H, Jia L-J, Lin Y-A, Xiang P. Effects of interface conditions on tribological and hysteretic behaviors of symmetric friction connections. Eng Struct 2024;302:117405. http://dx.doi.org/10.1016/j.engstruct.2023.117405.
[15] Li H-N, Yin Y-W, Wang S-Y. Studies on seismic reduction of story-incresed buildings with friction layer and energy-dissipated devices. Earthq Eng Struct Dyn 2003;32(14):2143–60. http://dx.doi.org/10.1002/eqe.320.
[16] Morgen BG, Kurama YC. Characterization of two friction interfaces for use in seismic damper applications. Mater Struct 2009;42(1):35–49. http://dx.doi.org/10.1617/s11527-008-9365-y.
[17] Chan RW, Tang W. Serviceability conditions of friction dampers for seismic risk mitigations. Structures 2022;35:500–10. http://dx.doi.org/10.1016/j.istruc.2021.11.033.
[18] Minimum design loads and associated criteria for buildings and other structures (ASCE/SEI 7-22). American Society of Civil Engineers; 2022.
[19] Lie MT. Earthquake energy absorbers (Master thesis), University of Wollongong; 1983.
[20] Tyler RG. Test on a brake lining damper for structures. Bull N. Z Soc Earthq Eng 1985;18(3):280–4. http://dx.doi.org/10.5459/bnzsee.18.3.280-284.

[21] Kim H-J, Christopoulos C. Friction damped posttensioned self-centering steel moment-resisting frames. J Struct Eng 2008;134(11):1768–79. http://dx.doi.org/10.1061/(ASCE)0733-9445(2008)134:11(1768).
[22] Kim HJ. Self-centering steel moment-resisting frames with energy dissipating systems (Ph.D. thesis), University of Toronto; 2007.
[23] Golondrino JC, MacRae GA, Chase JG, Rodgers GW, Clifton GC. Application of brake pads on asymmetrical friction connection (AFC). In: Proceedings of the 2013 NZSEE Annual Technical Conference. New Zealand Society for Earthquake Engineering; 2013.
[24] Tsampras G, Sause R. Development and experimental validation of deformable connection for earthquake-resistant building systems with reduced floor accelerations. Technical Report, Lehigh University; 2015.
[25] Bowden F, Tabor D. The friction and lubrication of solids. Oxford University Press; 2001.
[26] Li Z, He M, Dong H, Shu Z, Wang X. Friction performance assessment of Non-Asbestos Organic (NAO) composite-to-steel interface and Polytetrafluoroethylene (PTFE) composite-to-steel interface: Experimental evaluation and application in seismic resistant structures. Constr Build Mater 2018;174:272–83. http://dx.doi.org/10.1016/j.conbuildmat.2018.04.096.
[27] Paronesso M, Lignos DG. Experimental study of sliding friction damper with composite materials for earthquake resistant structures. Eng Struct 2021;248:113063. http://dx.doi.org/10.1016/j.engstruct.2021.113063.
[28] Gao J, Yuan Y, Qiu T, Wang C-L, Qu Z. Performance optimization and loading rate-dependency of friction dampers with non-metallic friction materials. J Build Eng 2022;54:104609. http://dx.doi.org/10.1016/j.jobe.2022.104609.
[29] Blau PJ. Friction science and technology: from concepts to applications. Boca Raton, FL: CRC Press; 2009.
[30] Latour M, Piluso V, Rizzano G. Free from damage beam-to-column joints: Testing and design of DST connections with friction pads. Eng Struct 2015;85:219–33. http://dx.doi.org/10.1016/j.engstruct.2014.12.019.
[31] Coulomb CA. Théorie des machines simples (theory of simple machines). Paris: Bachelier; 1821.
[32] Thoppul SD, Gibson RF, Ibrahim RA. Phenomenological modeling and numerical simulation of relaxation in bolted composite joints. J Compos Mater 2008;42(17):1709–29. http://dx.doi.org/10.1177/0021998308092544.
[33] Caccese V, Berube KA, Fernandez M, Daniel Melo J, Kabche JP. Influence of stress relaxation on clamp-up force in hybrid composite-to-metal bolted joints. Compos Struct 2009;89(2):285–93. http://dx.doi.org/10.1016/j.compstruct.2008.07.031.
[34] Cox R. Engineered tribological composites. Warrendale, PA: SAE International; 2011, http://dx.doi.org/10.4271/R-401.
[35] Hentati N, Makni F, Elleuch R. Braking performance of friction materials: A review of manufacturing process impact and future trends. Tribol - Mater Surf Interfaces 2023;17(2):136–57. http://dx.doi.org/10.1080/17515831.2023.2216092.
[36] Nicholson G. Facts about friction: A friction material manual almost all you need to know about manufacturing. Gedoran; 1995.
[37] Tatara RA. Compression molding. In: Applied plastics engineering handbook. William Andrew; 2024, p. 389–424. http://dx.doi.org/10.1016/B978-0-323-88667-3.00011-4.
[38] Brake lining quality test procedure (SAE J661 202110). SAE International; 2021.
[39] Gatke. 2023, URL https://www.scanpac.com/gatke/. [Accessed 30 November 2023].
[40] Harvey tool. 2024, URL https://www.harveytool.com/. [Accessed 19 September 2024].
[41] Makita. 2024, URL https://www.makitatools.com/. [Accessed 19 September 2024].
[42] ASTM International. Standard Test Method for Tensile Properties of Plastics. ASTM D638-22, West Conshohocken, PA: ASTM International; 2022, http://dx.doi.org/10.1520/D0638-22.
[43] Barbero EJ. Introduction to composite materials design. CRC Press; 2010.
[44] MTS. 2024, URL https://www.mts.com/en. [Accessed 19 March 2024].
[45] ASTM International. Standard Test Method for Bearing Response of Polymer Matrix Composite Laminates. ASTM D5961/D5961M-23, West Conshohocken, PA: ASTM International; 2023, http://dx.doi.org/10.1520/D5961_D5961M-23.
[46] Steel construction manual. 15th ed.. American Institute of Steel Construction; 2017.
[47] Thoppul SD, Finegan J, Gibson RF. Mechanics of mechanically fastened joints in Polymer–Matrix composite structures – A review. Compos Sci Technol 2009;69(3):301–29. http://dx.doi.org/10.1016/j.compscitech.2008.09.037.
[48] Hytorc. 2024, URL https://hytorc.com/. [Accessed 19 September 2024].
[49] ASTM International. Standard Specification for Hardened Steel Backup and Reaction Washers Inch and Metric Dimensions. ASTM F3394/F3394M-23, West Conshohocken, PA: ASTM International; 2023, http://dx.doi.org/10.1520/F3394_F3394M-23.
[50] Bostik. 2024, URL https://www.bostik.com/us/en_US/. [Accessed 19 September 2024].
[51] Transducer techniques inc.. 2024, URL https://www.transducertechniques.com/. [Accessed 19 September 2024].
[52] Fujifilm. 2024, URL https://www.fujifilm.com/us/en. [Accessed 19 September 2024].
[53] Lee K, Tsampras G, Mayorga CF. Reinforced concrete core wall buildings with modified friction-based force-limiting connections: Connection design considerations and 3D response to bidirectional ground motions. J Struct Eng 2025;151(2):04024203. http://dx.doi.org/10.1061/JSENDH.STENG-13609.
[54] Schreier H, Orteu J-J, Sutton MA. Image correlation for shape, motion and deformation measurements: Basic concepts, theory and applications. Boston, MA: Springer US; 2009, http://dx.doi.org/10.1007/978-0-387-78747-3.
[55] Correlated-solutions. 2023, URL https://www.correlatedsolutions.com/. [Accessed 05 December 2023].
[56] Keyence. 2024, URL https://www.keyence.com/. [Accessed 20 September 2024].
[57] Blau PJ. On the nature of running-in. Tribol Int 2005;38(11–12):1007–12. http://dx.doi.org/10.1016/j.triboint.2005.07.020.
[58] Kragelsky IV, Dobychin MN, Kombalov VS. Friction and wear: calculation methods. Pergamon Press; 1982.
[59] Zhang X, Zhang L, Yu X, Zhu X, Tu Y, Kang X. A novel and quantitative determination method for the running-in process through dimensionless real contact area. Wear 2023;514:204554. http://dx.doi.org/10.1016/j.wear.2022.204554.
[60] Hsu S, Munro R, Shen M, Gates R. Boundary lubricated wear. In: Wear – materials, mechanisms and practice. John Wiley & Sons, Ltd; 2005, p. 37–70. http://dx.doi.org/10.1002/9780470017029.ch4.
[61] Song W, Gweon J, Park JS, Kim J, Kim J, Jang H. Role of contact plateaus on velocity-dependent friction of brake friction composite with steel fibres. Tribol Int 2022;171:107568. http://dx.doi.org/10.1016/j.triboint.2022.107568.
[62] Wen S, Huang P. Principles of tribology. Hoboken, NJ: Wiley; 2017.
[63] Park SB, Cho KH, Jung S, Jang H. Tribological properties of brake friction materials with steel fibers. Met Mater Int 2009;15:27–32. http://dx.doi.org/10.1007/s12540-009-0027-6.
[64] Kim JW, Joo BS, Jang H. The effect of contact area on velocity weakening of the friction coefficient and friction instability: A case study on brake friction materials. Tribol Int 2019;135:38–45. http://dx.doi.org/10.1016/j.triboint.2019.02.034.
[65] Dieterich JH, Kilgore BD. Direct observation of frictional contacts: New insights for state-dependent properties. Pure Appl Geophys 1994;143:283–302. http://dx.doi.org/10.1007/BF00874332.